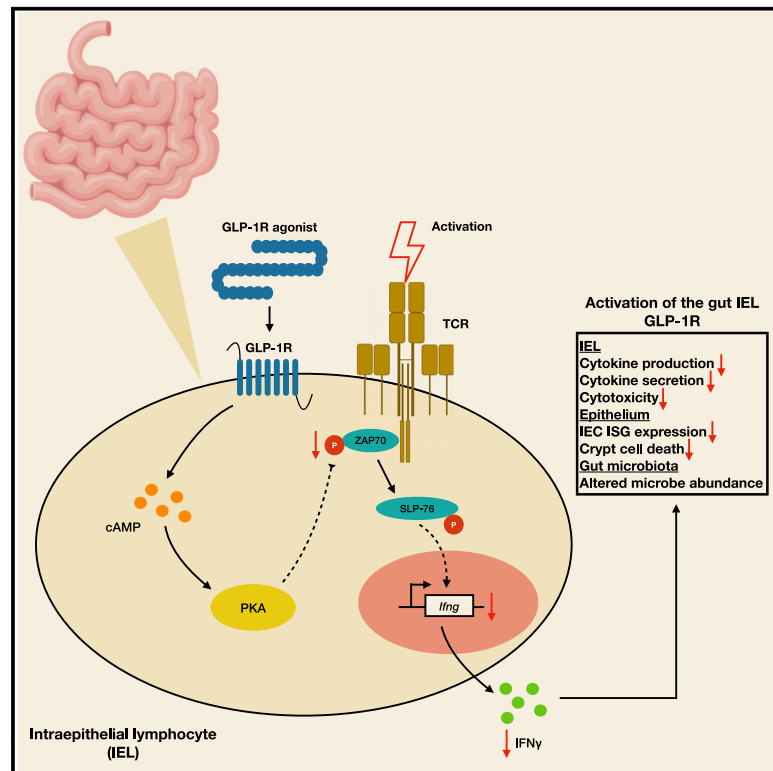# Divergent roles for the gut intraepithelial lymphocyte GLP-1R in control of metabolism, microbiota, and T cell-induced inflammation

Graphical abstract

Highlights

- The gut T cell GLP-1 receptor is not essential for metabolic homeostasis

- The IEL GLP-1R controls a subset of GLP-1 actions on microbiota

- T cell-dependent gut inflammation is attenuated by GLP-1 through the IEL GLP-1R

- GLP-1 attenuates LPS-induced inflammation independent of the IEL GLP-1R

Authors

Chi Kin Wong, Bernardo Yusta,
Jacqueline A. Koehler, ...,
Dianne Matthews, Randy J. Seeley,
Daniel J. Drucker

Correspondence

drucker@lunenfeld.ca

In brief

GLP-1 exerts incompletely understood anti-inflammatory actions, as most immune cells do not express the GLP-1R. Here, Wong et al. show that the intestinal intraepithelial lymphocyte GLP-1R is required for actions of GLP-1 on gut microbiota and for selective restraint of local and systemic T cell-induced, but not lipopolysaccharide-induced, inflammation.

Cell Metabolism

CellPress

Article

Divergent roles for the gut intraepithelial lymphocyte GLP-1R in control of metabolism, microbiota, and T cell-induced inflammation

Chi Kin Wong,[1] Bernardo Yusta,[1] Jacqueline A. Koehler,[1] Laurie L. Baggio,[1] Brent A. McLean,[1] Dianne Matthews,[1] Randy J. Seeley,[2] and Daniel J. Drucker[1,3,4,*]

[1]Lunenfeld-Tanenbaum Research Institute, Sinai Health System, Toronto, ON, Canada
[2]Department of Surgery, University of Michigan, Ann Arbor, MI, USA
[3]Department of Medicine, University of Toronto, Toronto, ON, Canada
[4]Lead contact
*Correspondence: drucker@lunenfeld.ca
https://doi.org/10.1016/j.cmet.2022.08.003

SUMMARY

Gut intraepithelial lymphocytes (IELs) are thought to calibrate glucagon-like peptide 1 (GLP-1) bioavailability, thereby regulating systemic glucose and lipid metabolism. Here, we show that the gut IEL GLP-1 receptor (GLP-1R) is not required for enteroendocrine L cell GLP-1 secretion and glucose homeostasis nor for the metabolic benefits of GLP-1R agonists (GLP-1RAs). Instead, the gut IEL GLP-1R is essential for the full effects of GLP-1RAs on gut microbiota. Moreover, independent of glucose control or weight loss, the anti-inflammatory actions of GLP-1RAs require the gut IEL GLP-1R to selectively restrain local and systemic T cell-induced, but not lipopolysaccharide-induced, inflammation. Such effects are mediated by the suppression of gut IEL effector functions linked to the dampening of proximal T cell receptor signaling in a protein-kinase-A-dependent manner. These data reposition key roles of the L cell-gut IEL GLP-1R axis, revealing mechanisms linking GLP-1R activation in gut IELs to modulation of microbiota composition and control of intestinal and systemic inflammation.

INTRODUCTION

The gut-derived hormone glucagon-like peptide 1 (GLP-1) acts on the pancreatic islets and the brain to lower blood glucose and reduce food intake and body weight, respectively (Müller et al., 2019). Collectively, these actions support the development of multiple GLP-1 receptor agonists (GLP-1RAs) for type 2 diabetes (T2D) and obesity (Drucker et al., 2017). GLP-1RAs also reduce rates of major adverse cardiovascular events (Sattar et al., 2021) and decrease inflammation (Drucker, 2018). The anti-inflammatory mechanisms of GLP-1RAs are not well understood, yet may contribute to the therapeutic activity of these agents in non-alcoholic steatohepatitis (NASH) (Newsome et al., 2021), atherosclerosis and cardiovascular disease (Noyan-Ashraf et al., 2013; Rakipovski et al., 2018), and neurodegenerative disorders (Athauda et al., 2017; Wang et al., 2021). Whether these anti-inflammatory effects are secondary to improved metabolic control, weight loss, or direct actions of GLP-1RAs on GLP-1R+ immune cell populations, remains uncertain.

Gut intraepithelial lymphocytes (IELs) are considered the first line of defense of the gut barrier, comprising mainly CD8+ T cells, and are further subclassified into natural IELs, which are derived directly from the thymus through agonist selection, and induced IELs, which arise after peripheral naive T cells encounter foreign antigens (Cheroutre et al., 2011). Gut IELs are one of the few immune cell populations known to express a functional GLP-1R (He et al., 2019; Yusta et al., 2015), and the proximity of GLP-1R+ gut IELs to GLP-1-producing L cells within the gut epithelium is consistent with a local enteroendocrine L cell-IEL axis. Remarkably, integrin β7 (Itgb7) knockout (KO) mice, which lack most gut IELs, or lethally irradiated mice reconstituted with a mix of $Itgb7^{-/-}$ and $Glp1r^{-/-}$ bone marrow, displayed improved glucose control and reduced atherosclerosis, attributed to enhanced circulating GLP-1 levels and increased L cell density (He et al., 2019). These findings implied that the gut IEL GLP-1R limits the bioavailability of GLP-1 from L cells, whereas loss of the gut IEL GLP-1R improves metabolism by augmenting GLP-1 secretion (He et al., 2019; Khan et al., 2021).

Consistent with a role for L cells as pathogen sensors, proinflammatory and microbial signals also induce GLP-1 secretion (Drucker, 2018; Lebrun et al., 2017; Martchenko et al., 2020; Psichas et al., 2015; Yoon et al., 2021). In turn, GLP-1 influences local, systemic, or central nervous system (CNS) inflammation through the gut-brain axis (Gribble and Reimann, 2016; Heiss et al., 2021). GLP-1 also modulates the composition of the gut microbiota in animals and humans with T2D (Wang et al., 2018;

CellPress

Cell Metabolism
Article
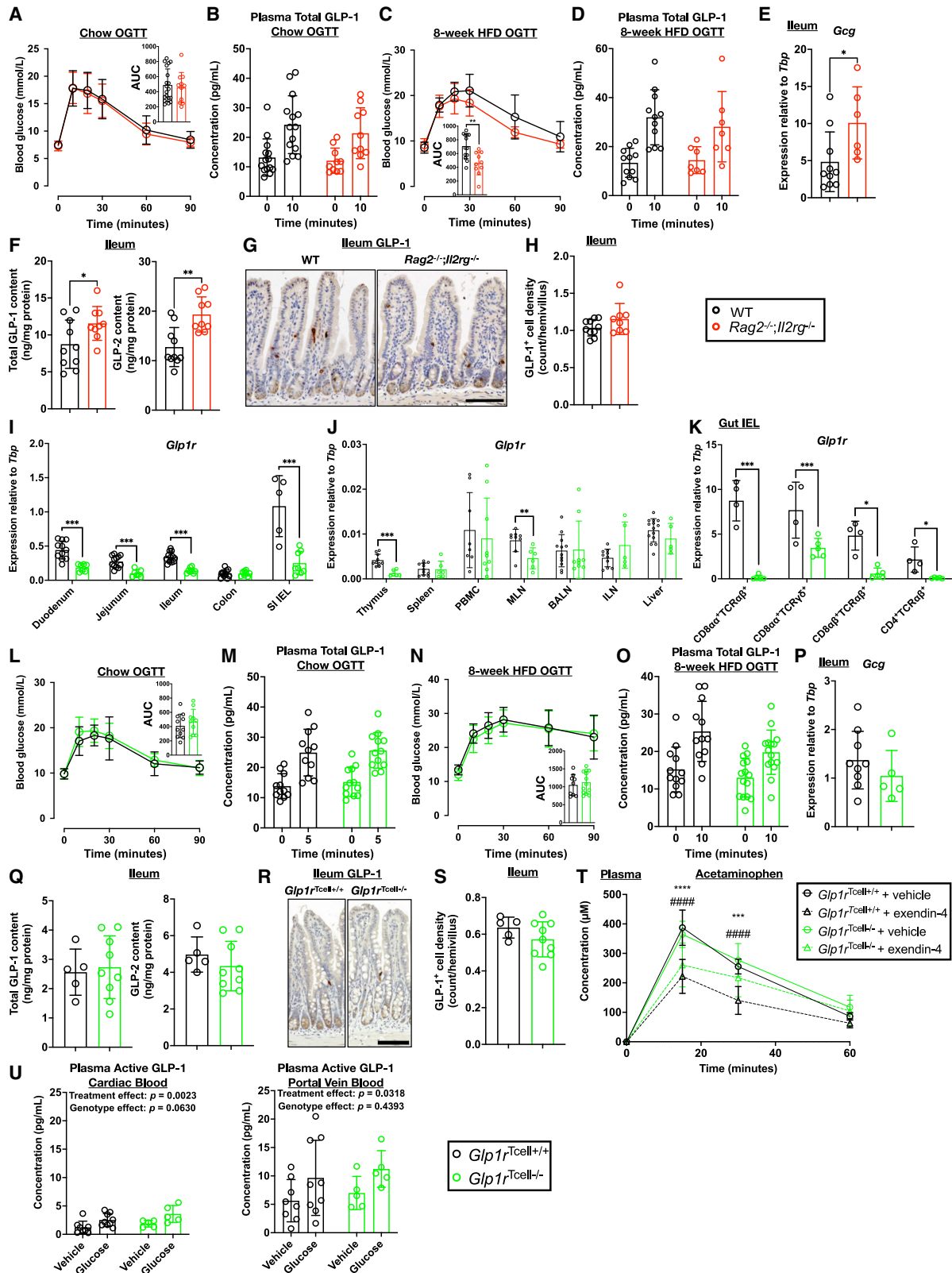
Figure 1. Gut IELs and the gut IEL GLP-1R are dispensable for GLP-1 secretion prior to or during metabolic challenges

(A) Blood glucose levels during OGTTs and AUC of the tests in chow-fed WT and $Rag2^{-/-}$; $Il2rg^{-/-}$ mice fasted for 5 h and gavaged with glucose (2 g/kg). n = 11–19.

Cell Metabolism
Article

CellPress

Zhao et al., 2018), changes that may contribute to the metabolic benefits of GLP-1R agonism (Charpentier et al., 2021; Kim et al., 2021). GLP-1 may alter microbiota via the indirect impact of improved glucose control, weight loss, changes in gut motility, or alteration of immune function and microbiota-epithelial-lymphocyte interactions. Although $Glp1r^{-/-}$ mice exhibit a shift in gut microbiota representation (Yusta et al., 2015), the relative importance and identity of GLP-1R$^+$ cell types impacting the gut microbiota have not been determined.

Hematopoietic-derived immune cell lineages are also potential direct targets for the anti-inflammatory actions of GLP-1RAs, although the spleen, thymus, and peripheral lymph nodes express very low levels of $Glp1r$ (Heng et al., 2008) and do not respond robustly upon GLP-1R activation (Hadjiyanni et al., 2010). Acute activation of the gut IEL GLP-1R also dampens cytokine expression, contributing to attenuation of gut inflammation (Yusta et al., 2015). Although studies have highlighted the importance of anti-inflammatory and metabolic actions of GLP-1 (Müller et al., 2019), the specific contribution(s) of the gut IEL GLP-1R for the control of metabolism versus T cell immune function has not been examined.

To interrogate the metabolic importance of GLP-1R$^+$ IELs, we studied $Rag2^{-/-};Il2rg^{-/-}$ mice and generated mice lacking T cell GLP-1Rs ($Glp1r^{Tcell-/-}$). Surprisingly, inactivation of the gut IEL GLP-1R did not impair control of GLP-1 secretion and was dispensable for the metabolic benefits of GLP-1RAs. Instead, the gut IEL GLP-1R was required for the actions of GLP-1RAs to modulate a subset of the gut microbiota and suppress systemic and gut inflammation initiated from T cell activation *in vivo*. Notably, GLP-1RAs inhibited gut IEL effector functions in part by dampening their proximal T cell receptor (TCR) signaling in a protein kinase A (PKA)-dependent manner. These data link the gut

IEL GLP-1R signaling within the gut immune compartment to the control of microbial populations and suppression of local and systemic inflammation.

RESULTS

Loss of lymphocytes, including gut IELs, in $Rag2^{-/-};Il2rg^{-/-}$ mice does not change GLP-1 secretion prior to and during metabolic challenges

$Glp1r$ expression has been localized to unconventional T cells, including gut IELs (Yusta et al., 2015), and hepatic $\gamma\delta^+$ T cells (McLean et al., 2021a). To extend the importance of data implicating gut IELs in the control of GLP-1 secretion (He et al., 2019), we investigated the role of the gut IEL GLP-1R using several mouse models. We first examined $Rag2^{-/-};Il2rg^{-/-}$ mice, on a BALB/c background, which lack all lymphoid lineages including B cells, T cells, NK cells, and innate lymphoid cells (Song et al., 2010). $Rag2^{-/-};Il2rg^{-/-}$ mice exhibited ~90% reduction in the frequency of CD3$^+$ IELs in the small intestine, as shown by flow cytometry (Figure S1A). The duodenum of $Rag2^{-/-};Il2rg^{-/-}$ mice expressed no $Cd3g$, and levels of $Glp1r$ mRNA transcripts were reduced by 60% (Figure S1B). These findings are consistent with the predicted contribution of IELs, versus enteric neurons and Brunner's glands, to total gut $Glp1r$ expression in the small intestine (McLean et al., 2021a; Varin et al., 2019; Yusta et al., 2015).

Regular chow-fed $Rag2^{-/-};Il2rg^{-/-}$ mice displayed normal glucose tolerance (Figure 1A). Surprisingly, despite loss of the gut IEL population, circulating levels of total GLP-1 were not different upon oral glucose administration (Figure 1B). Similarly, oral gavage of olive oil induced comparable GLP-1 excursions in control versus R$ag2^{-/-};Il2rg^{-/-}$ mice (Figure S1C). Plasma

(B) Plasma total GLP-1 levels of chow-fed WT and $Rag2^{-/-}$; $Il2rg^{-/-}$ mice after a 5-h fast followed by gavaging of glucose (2 g/kg). n = 10–14.

(C) Blood glucose levels during OGTTs and AUC of the tests in WT and $Rag2^{-/-}$; $Il2rg^{-/-}$ mice after 8 weeks of HFD feeding, fasted for 5 h, and gavaged with glucose (2 g/kg). n = 10–13.

(D) Plasma total GLP-1 levels of WT and $Rag2^{-/-}$; $Il2rg^{-/-}$ mice after 8 weeks of HFD feeding subsequent to a 5-h fast followed by gavaging of glucose (2 g/kg). n = 7–11.

(E) Expression of Gcg in chow-fed WT and $Rag2^{-/-}$; $Il2rg^{-/-}$ mouse ilea. n = 6–9.

(F) Left panel: total GLP-1 content of WT and $Rag2^{-/-}$; $Il2rg^{-/-}$ mouse ilea. Right panel: GLP-2 content of WT and $Rag2^{-/-}$; $Il2rg^{-/-}$ mouse ilea. n = 9 or 10.

(G) Representative images of GLP-1 staining in WT and $Rag2^{-/-}$; $Il2rg^{-/-}$ mouse ilea by immunohistochemistry. Scale bar, 100 μm.

(H) Density of GLP-1$^+$ cells in WT and $Rag2^{-/-}$; $Il2rg^{-/-}$ mouse ilea stained for GLP-1 by immunohistochemistry. n = 8–10.

(I–K) Expression of $Glp1r$ in (I) the gut, (J) lymphoid tissues and the liver, and (K) FACS-purified IEL subpopulations of $Glp1r^{Tcell+/+}$ and $Glp1r^{Tcell-/-}$ mice. n = 4–14.

(L) Blood glucose levels during OGTTs and AUC of the tests in chow-fed $Glp1r^{Tcell+/+}$ and $Glp1r^{Tcell-/-}$ mice fasted for 5 h and gavaged with glucose (2 g/kg). n = 10 or 11.

(M) Plasma total GLP-1 levels of chow-fed $Glp1r^{Tcell+/+}$ and $Glp1r^{Tcell-/-}$ mice after a 5-h fast followed by gavaging of glucose (2 g/kg). n = 11 or 12.

(N) Blood glucose levels during OGTTs and AUC of the tests in $Glp1r^{Tcell+/+}$ and $Glp1r^{Tcell-/-}$ mice after 8 weeks of HFD feeding, fasted for 5 h, and gavaged with glucose (2 g/kg). n = 9–13.

(O) Plasma total GLP-1 levels from $Glp1r^{Tcell+/+}$ and $Glp1r^{Tcell-/-}$ mice after 8 weeks of HFD feeding after a 5-h fast followed by gavaging of glucose (2 g/kg). n = 12–15.

(P) Expression of Gcg in $Glp1r^{Tcell+/+}$ and $Glp1r^{Tcell-/-}$ mouse ilea. n = 5–9.

(Q) Left panel: total GLP-1 content of $Glp1r^{Tcell+/+}$ and $Glp1r^{Tcell-/-}$ mouse ilea. Right panel: GLP-2 content of $Glp1r^{Tcell+/+}$ and $Glp1r^{Tcell-/-}$ mouse ilea. n = 5–9.

(R) Representative images of GLP-1 staining of $Glp1r^{Tcell+/+}$ and $Glp1r^{Tcell-/-}$ mouse ilea by immunohistochemistry. Scale bar, 100 μm.

(S) Density of GLP-1$^+$ cells in $Glp1r^{Tcell+/+}$ and $Glp1r^{Tcell-/-}$ mouse ilea stained for GLP-1 by immunohistochemistry. n = 5–9.

(T) Plasma acetaminophen concentrations in fasted $Glp1r^{Tcell+/+}$ and $Glp1r^{Tcell-/-}$ mice after gavaging with acetaminophen (100 mg/kg). n = 5 or 6.

(U) Active GLP-1 levels in cardiac blood plasma (left panel) and hepatic portal vein blood plasma (right panel) from mice pretreated with sitagliptin (400 μg/mouse) for 30 min followed by gavaging with vehicle (water) or glucose (2 g/kg). n = 5–9.

Data are represented as mean ± SD. * p < 0.05, ** p < 0.01, and *** p < 0.001. For (T), *** p < 0.001 and **** p < 0.0001 between vehicle-treated and semaglutide-treated $Glp1r^{Tcell+/+}$ mice; #### p < 0.0001 between vehicle-treated and semaglutide-treated $Glp1r^{Tcell-/-}$ mice. Student's t tests were used in (C), (E), (F), (I), (J), and (K). Two-way ANOVA tests were used in (U). Repeated measure ANOVA tests were used in (T).

Abbreviations: AUC, area under curve; OGTT, oral glucose tolerance test; HFD, high-fat diet; Gcg, glucagon; SI IELs, small intestine intraepithelial lymphocytes; MLNs, mesenteric lymph nodes; PBMCs, peripheral blood mononuclear cells; BALNs, brachioaxillary lymph nodes; ILNs, inguinal lymph nodes.

free fatty acid levels were not different in $Rag2^{-/-};Il2rg^{-/-}$ mice during the lipid tolerance test but plasma triglycerides were reduced in fasted $Rag2^{-/-};Il2rg^{-/-}$ mice (Figure S1C). Intriguingly, high-fat diet (HFD)-fed $Rag2^{-/-};Il2rg^{-/-}$ mice showed improved oral glucose tolerance (Figure 1C); however, GLP-1 levels in HFD-fed $Rag2^{-/-};Il2rg^{-/-}$ mice were not different before or after a glucose challenge (Figure 1D). Glucose-stimulated insulin responses were comparable in HFD-fed control versus $Rag2^{-/-};Il2rg^{-/-}$ mice (Figure S1D). HFD-fed $Rag2^{-/-};Il2rg^{-/-}$ mice also displayed improved intraperitoneal glucose tolerance and insulin tolerance (Figures S1E and S1F). Body weight was normal in $Rag2^{-/-};Il2rg^{-/-}$ mice after 12 weeks of HFD feeding (Figure S1G); however, fat mass was higher and lean mass was reduced (Figure S1H). Energy expenditure, locomotor activity, and food and water intake were not different (Figures S1I–S1K). The higher fat and lower lean mass of HFD-fed $Rag2^{-/-};Il2rg^{-/-}$ mice reflected higher gonadal white adipose tissue weight and lower liver, spleen, and gut weight, respectively (Figure S1L). Hence, $Rag2^{-/-};Il2rg^{-/-}$ mice deficient in gut T cells phenocopied a subset of metabolic findings in $Itgb7^{-/-}$ mice (He et al., 2019; Luck et al., 2015).

Higher plasma GLP-1 levels were associated with enhanced gut glucagon gene (Gcg) expression and greater L cell density in the ileum of $Itgb7^{-/-}$ mice (He et al., 2019). $Rag2^{-/-};Il2rg^{-/-}$ mice also exhibited higher Gcg expression and total GLP-1 and GLP-2 content in the ileum (Figures 1E and 1F), but ileal L cell density was not different (Figures 1G and 1H). Together with findings of normal circulating levels of GLP-1, the improved glucose tolerance in HFD-fed $Rag2^{-/-};Il2rg^{-/-}$ mice lacking gut IELs does not reflect increased GLP-1 bioactivity.

Lck-Cre efficiently inactivates the GLP-1R in gut IELs

To extend our findings from $Rag2^{-/-};Il2rg^{-/-}$ mice to a more selective model retaining immune cell populations yet exhibiting disruption of T cell and gut IEL GLP-1R expression, we crossed mice harboring *Lck-Cre* (Hennet et al., 1995) with *Glp1r* flox/flox ($Glp1r^{fl/fl}$) mice to generate $Glp1r^{Tcell-/-}$ mice on a C57BL/6J background. $Glp1r$ expression was reduced within the duodenum, jejunum, and ileum of $Glp1r^{Tcell-/-}$ mice by at least 60% (Figure 1I), whereas colonic $Glp1r$ expression was not different in $Glp1r^{Tcell+/+}$ versus $Glp1r^{Tcell-/-}$ mice. $Glp1r$ expression was enriched within isolated small bowel IELs relative to mRNA levels in isolated small bowel segments and markedly reduced by more than 75% in the gut IELs isolated from $Glp1r^{Tcell-/-}$ mice (Figure 1I).

Much lower levels of $Glp1r$ mRNA were detected in other immune organs, with knockdown of $Glp1r$ mRNA observed in the thymus and mesenteric lymph nodes (MLNs) from $Glp1r^{Tcell-/-}$ mice (Figure 1J). Expression of $Glp1r$ in the spleen, peripheral blood mononuclear cells (PBMCs), and brachioaxillary and inguinal lymph nodes was not reduced in $Glp1r^{Tcell-/-}$ mice (Figure 1J). Although hepatic $\gamma\delta$ T cells express $Glp1r$ (McLean et al., 2021a), we did not detect a reduction of $Glp1r$ mRNA transcripts in the liver of $Glp1r^{Tcell-/-}$ mice (Figure 1J), likely reflecting the low abundance of hepatic $\gamma\delta$ T cells and the decreased efficiency of the proximal *Lck* promoter in driving recombination in $\gamma\delta$ T cells (Fiala et al., 2019). Expression of $Glp1r$ in lungs and atria of $Glp1r^{Tcell-/-}$ mice was normal (Figure S1M).

Natural IELs can be either TCR$\alpha\beta^+$ or TCR$\gamma\delta^+$ and acquire CD8$\alpha\alpha$ expression after homing to the gut, whereas induced

IELs are mostly CD8$\alpha\beta^+$TCR$\alpha\beta^+$ with a subset identified as CD4$^+$TCR$\alpha\beta^+$ (Cheroutre et al., 2011). We sorted gut IELs into natural and induced IELs based on their CD8 dimer expression by fluorescence-activated cell sorting (FACS). In cells isolated from the small bowel of $Glp1r^{Tcell-/-}$ mice, $Glp1r$ expression was lower in both natural (CD8$\alpha\alpha^+$) and induced (CD8$\alpha\beta^+$ or CD4$^+$) IELs but virtually extinguished in TCR$\alpha\beta^+$ cells (Figure 1K). Of note, $Glp1r$ mRNA transcripts in CD8$\alpha\alpha^+$TCR$\gamma\delta^+$ IELs from $Glp1r^{Tcell-/-}$ mice were reduced by only 50% (Figure 1K), consistent with the lower efficiency of the proximal *Lck* promoter in targeting $\gamma\delta$ T cells (Fiala et al., 2019). Despite the loss of $Glp1r$ expression in gut IELs, jejunal T cell density was normal in $Glp1r^{Tcell-/-}$ mice (Figure S1N). Moreover, the relative abundance of most gut IEL subtypes was unchanged (Figures S1O and S1P), although the population of CD8$\alpha\alpha^{+-}$ TCR$\gamma\delta^+$ IELs was slightly expanded in $Glp1r^{Tcell-/-}$ mice (Figure S1P). Hence, $Glp1r^{Tcell-/-}$ mice exhibit efficient deletion of $Glp1r$ in most gut IELs while preserving IEL abundance and immunophenotypes.

Loss of *Glp1r* in gut IELs does not affect GLP-1 secretion with or without metabolic challenges

The defective development of gut IELs in $Itgb7^{-/-}$ mice increased levels of GLP-1 and improved glucose tolerance, attributed to loss of the gut IEL GLP-1R (He et al., 2019). Nevertheless, chow-fed $Glp1r^{Tcell-/-}$ mice displayed normal oral glucose tolerance (Figure 1L), with GLP-1 and insulin levels increasing to a similar extent in $Glp1r^{Tcell+/+}$ versus $Glp1r^{Tcell-/-}$ mice during the oral glucose tolerance test (OGTT) (Figures 1M and S1Q). Unlike $Rag2^{-/-};Il2rg^{-/-}$ mice, $Glp1r^{Tcell-/-}$ mice did not show improved oral glucose tolerance compared with $Glp1r^{Tcell+/+}$ mice after 8 weeks of HFD feeding (Figure 1N). The total GLP-1 and insulin responses during the OGTT were unchanged in HFD-fed $Glp1r^{Tcell-/-}$ mice (Figures 1O and S1R). Furthermore, intraperitoneal glucose tolerance and insulin tolerance were not different in $Glp1r^{Tcell+/+}$ versus $Glp1r^{Tcell-/-}$ mice (Figures S1S and S1T). Body weight gain was comparable (Figure S1U), but HFD-fed $Glp1r^{Tcell-/-}$ mice had slightly reduced fat mass (Figure S1V). HFD-fed $Glp1r^{Tcell-/-}$ mice gained relatively more body weight than HFD-fed $Rag2^{-/-};Il2rg^{-/-}$ mice on a BALB/c background over the same 12-week period of HFD feeding (Figures S1G and S1U), consistent with the increased susceptibility to diet-induced obesity in mice on a C57BL/6J background (Montgomery et al., 2013). Energy expenditure, locomotor activity, and food intake were normal, and water intake was mildly reduced in HFD-fed $Glp1r^{Tcell-/-}$ mice (Figures S1W, S1X, and S1Y). $Glp1r^{Tcell-/-}$ mice exhibited normal Gcg expression, total GLP-1 and GLP-2 content, and L cell density in the ileum (Figures 1P–1S).

The gut-brain GLP-1 axis also regulates gut motility (Imeryüz et al., 1997), hence we tested gastric emptying responses in $Glp1r^{Tcell-/-}$ mice by administering acetaminophen. $Glp1r^{Tcell+/+}$ and $Glp1r^{Tcell-/-}$ mice exhibited similar gastric emptying profiles (Figure 1T). Exendin-4 suppressed gastric emptying effectively in both genotypes, suggesting that the gut IEL GLP-1R is not required for the control of gastric emptying (Figure 1T). Because the portal vein blood contains a substantial proportion of active GLP-1 secreted from L cells and potentially reflects sequestration by gut IELs, we assessed portal GLP-1 levels in

Cell Metabolism
Article

CellPress
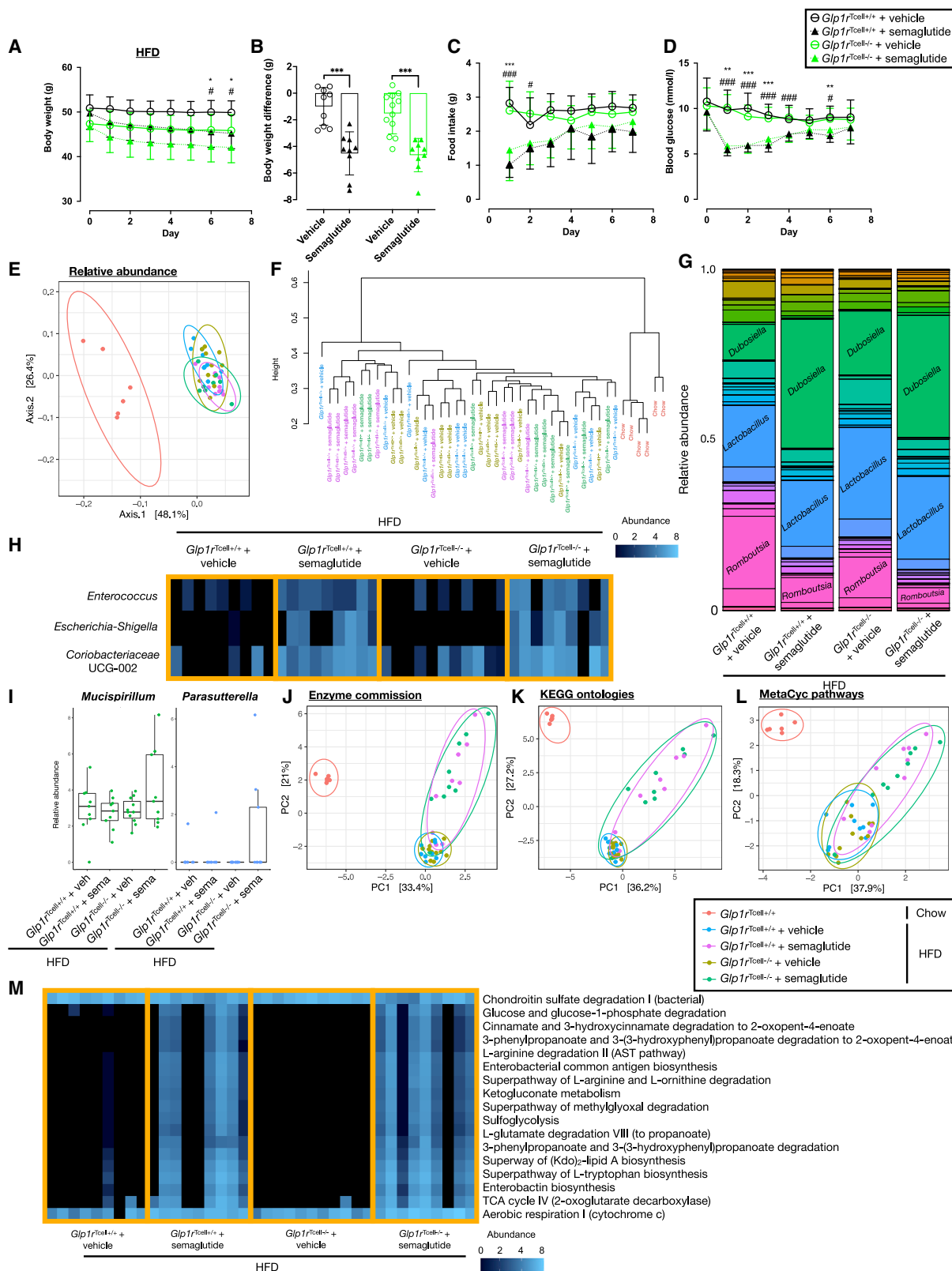
Figure 2. Loss of the GLP-1R in gut IELs preserves the metabolic benefits but modifies the gut microbiota-altering effects of semaglutide

(A) Body weight of HFD-fed $Glp1r^{Tcell+/+}$ and $Glp1r^{Tcell-/-}$ mice over 1 week of daily semaglutide (10 μg/kg) treatment. The body weight of these HFD-fed animals prior to semaglutide treatment is reported in Figure S1U. Solid lines and dotted lines denote vehicle and semaglutide treatment, respectively. n = 8 or 9.

(legend continued on next page)

$Glp1r^{Tcell-/-}$ mice. Active GLP-1 levels were increased following a bolus of glucose and were higher in portal vein versus cardiac blood (Figure 1U). However, active GLP-1 levels in cardiac and portal vein blood were not different in $Glp1r^{Tcell+/+}$ versus $Glp1r^{Tcell-/-}$ mice with or without glucose challenge. Overall, deletion of $Glp1r$ in T cells, including gut IELs, neither enhances the number of L cells and GLP-1 levels nor improves oral glucose tolerance.

Loss of the GLP-1R in gut IELs preserves metabolic benefits but modifies the gut microbiota-altering effects of semaglutide

GLP-1RAs also attenuate systemic and tissue inflammation in animals and humans (Chaudhuri et al., 2012; Drucker, 2018; Heiss et al., 2021; Helmstädter et al., 2020; McLean et al., 2021a; Noyan-Ashraf et al., 2013; Sato et al., 2020). Nevertheless, GLP-1R expression is very low in many immune organs and cell types (Hadjiyanni et al., 2010; Heng et al., 2008; McLean et al., 2021b). To examine the role of the gut IEL GLP-1R in mediating the metabolic and anti-inflammatory actions of GLP-1RAs, we placed $Glp1r^{Tcell+/+}$ and $Glp1r^{Tcell-/-}$ mice on a HFD for 13 weeks and treated them with saline or semaglutide once daily for the last 7 days.

Body weight was slightly lower in saline-treated HFD-fed $Glp1r^{Tcell-/-}$ mice over the last week of HFD feeding (Figure 2A), although 1 week of semaglutide treatment reduced body weight, food intake, and blood glucose to a similar extent in both genotypes (Figures 2B–2D). The weight of subcutaneous white adipose tissue and interscapular brown adipose tissue, but not gonadal white adipose tissue, was reduced or trended lower with semaglutide treatment in both HFD-fed $Glp1r^{Tcell+/+}$ and $Glp1r^{Tcell-/-}$ mice (Figure S2A). Liver weight was also lower in semaglutide-treated mice (Figure S2A). Circulating levels of plasma cytokines and chemokines were similar across genotypes and semaglutide treatment (Figure S2B). Furthermore, the consequences of semaglutide treatment in the HFD-fed mouse liver, evident through downregulation of $Abcg1$, $Ccl2$, and Tnf mRNA transcripts (Figure S2C), were

preserved in $Glp1r^{Tcell-/-}$ mice. Moreover, semaglutide did not influence the gut IEL immunophenotype in either $Glp1r^{Tcell+/+}$ or $Glp1r^{Tcell-/-}$ mice on a HFD (Figure S2D).

The gut microbiota influences gut GLP-1 secretion, which in turn modulates local and systemic inflammation (Chimerel et al., 2014; Heiss et al., 2021; Hwang et al., 2015; Lebrun et al., 2017; Wichmann et al., 2013; Yadav et al., 2013). Hence, we performed 16s rRNA gene sequencing to characterize the fecal microflora in HFD-fed $Glp1r^{Tcell+/+}$ and $Glp1r^{Tcell-/-}$ mice treated with semaglutide. Clustering of microbiota samples by principal coordinates analysis or by hierarchical clustering pinpointed HFD feeding as the primary influence on the differences in beta diversity across groups (Figures 2E and 2F). Notably, semaglutide had minimal impact on the relative abundance of the microbiota, irrespective of the genotypes. The abundance of most genera of microbes was similar between the saline-treated and semaglutide-treated groups, although the abundance of some genera such as $Dubosiella$ and $Romboutsia$ were altered in the latter (Figure 2G). Differential abundance analysis by either DESeq2 and linear discriminant analysis effect size (LEfSe) commonly identified three genera of microbes induced by semaglutide in both HFD-fed $Glp1r^{Tcell+/+}$ and $Glp1r^{Tcell-/-}$ mice: $Enterococcus$, $Escherichia$-$Shigella$, and $Coriobacteriaceae$ UCG-002 (Figure 2H; Tables S1 and S2). Interestingly, some genera of commensal bacteria, such as $Mucispirillum$ and $Parasutterella$, were induced specifically by semaglutide in the gut of HFD-fed $Glp1r^{Tcell-/-}$ mice, but not in $Glp1r^{Tcell+/+}$ mice (Figure 2I; Table S1). We also performed prediction of the metagenome functions by phylogenetic investigation of communities by reconstruction of unobserved states 2 (PICRUSt2) (Douglas et al., 2020). Similar to the microbial relative abundance, the HFD exerted the strongest influence on the microbial functional abundance mapped to Enzyme Commission (EC) numbers, Kyoto Encyclopedia of Genes and Genomes (KEGG) ontologies, and pathways enriched for the EC numbers (MetaCyc pathways) (Figures 2J–2L). Semaglutide treatment had moderate effects on the functional abundance associated

(B) Body weight differences between $Glp1r^{Tcell+/+}$ and $Glp1r^{Tcell-/-}$ mice from day 0 to 7 of the daily semaglutide (10 µg/kg) treatment. n = 8 or 9.

(C) Food intake of HFD-fed $Glp1r^{Tcell+/+}$ and $Glp1r^{Tcell-/-}$ mice over 1 week of daily semaglutide (10 µg/kg) treatment. n = 6–9.

(D) Blood glucose of HFD-fed $Glp1r^{Tcell+/+}$ and $Glp1r^{Tcell-/-}$ mice as measured at 10 a.m. every day over 1 week of daily semaglutide (10 µg/kg) treatment. n = 8 or 9.

(E) A PCoA plot showing the similarity of microbiota profiles at the phylum level from fecal samples of HFD-fed $Glp1r^{Tcell+/+}$ and $Glp1r^{Tcell-/-}$ mice after 1 week of semaglutide (10 µg/kg) treatment. n = 6–11.

(F) A dendrogram showing hierarchical clustering of the gut microbiota samples of HFD-fed $Glp1r^{Tcell+/+}$ and $Glp1r^{Tcell-/-}$ mice after 1 week of semaglutide (10 µg/kg) treatment. The clustering was performed using weighted pair group method with arithmetic mean.

(G) Microbiota distribution at the genus level in fecal samples from HFD-fed $Glp1r^{Tcell+/+}$ and $Glp1r^{Tcell-/-}$ mice after 1 week of semaglutide (10 µg/kg) treatment.

(H) A heatmap highlighting selected microbe species differentially represented in the fecal samples of HFD-fed $Glp1r^{Tcell+/+}$ and $Glp1r^{Tcell-/-}$ mice after 1 week of semaglutide (10 µg/kg) treatment. Each column corresponds to one sample. n = 8–11.

(I) A boxplot and whisker plot showing selected microbe species differentially represented in the fecal samples of HFD-fed $Glp1r^{Tcell+/+}$ and $Glp1r^{Tcell-/-}$ mice after 1 week of semaglutide (10 µg/kg) treatment. n = 8–11.

(J–L) A PCoA plot showing clustering of the gut microbiota samples of HFD-fed $Glp1r^{Tcell+/+}$ and $Glp1r^{Tcell-/-}$ mice after 1 week of semaglutide (10 µg/kg) treatment based on their functional abundances associated with various (J) Enzyme Commission numbers, (K) KEGG ontologies, or (L) MetaCyc pathways. n = 6–11.

(M) A heatmap highlighting inferred pathways differentially abundant in the fecal samples of HFD-fed $Glp1r^{Tcell+/+}$ and $Glp1r^{Tcell-/-}$ mice after 1 week of semaglutide (10 µg/kg) treatment. Each column corresponds to one sample. n = 8–11.

Data are represented as mean ± SD. * $p < 0.05$, ** $p < 0.01$, and *** $p < 0.001$ between vehicle-treated and semaglutide-treated $Glp1r^{Tcell+/+}$ mice. # $p < 0.05$ and ### $p < 0.001$ between vehicle-treated and semaglutide-treated $Glp1r^{Tcell-/-}$ mice. Repeated measure ANOVA tests were used in (A), (C), and (D). Two-way ANOVA tests were used in (B).

Abbreviations: PCoA, principal coordinates analysis; veh, vehicle; sema, semaglutide.

Cell Metabolism
Article

CellPress
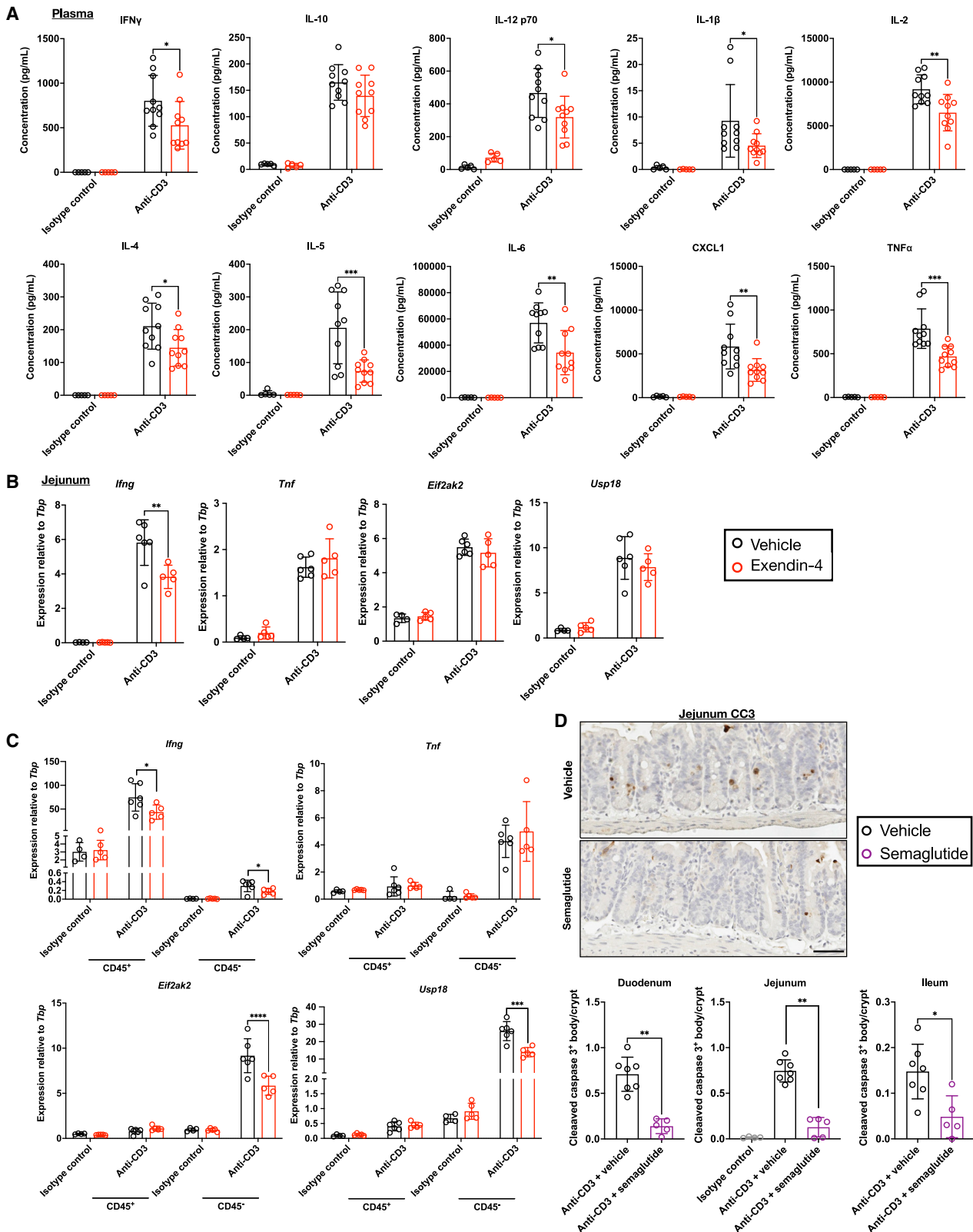
Figure 3. GLP-1R activation reduces intestinal IFN-γ responses driven by activated T cells

(A) Plasma cytokine levels in C57BL/6J mice treated with anti-CD3 and exendin-4 (10 nmol/kg) for 3 h. n = 5–10.

(B) Expression of *Ifng*, *Tnf*, *Eif2ak2*, and *Usp18* in the jejunum of C57BL/6J mice treated with anti-CD3 and exendin-4 (10 nmol/kg) for 3 h. n = 4–6.

(legend continued on next page)

with these ontologies, whereas genotypes had no overt effect (Figures 2J–2L). Focusing our analysis on the pathway abundance, semaglutide induced numerous pathways in both HFD-fed $Glp1r^{Tcell+/+}$ and $Glp1r^{Tcell-/-}$ mouse fecal microbiota, including pathways associated with nutrient metabolism (L-arginine, L-ornithine, L-glutamate, and glucose degradation; L-tryptophan biosynthesis), aromatic compound metabolism (3-phenylpropanoate, cinnamate, and 4-hydroxyphenylacetate degradation), and synthesis of other bacterial products (enterobactin and $(Kdo)_2$-lipid A biosynthesis) (Figure 2M). These findings were likely driven by the higher abundance of *Escherichia-Shigella* in the semaglutide-treated mice, because many of these pathways are associated with *Escherichia coli* metabolism (Manso et al., 2009; Raetz et al., 2007). HFD-fed $Glp1r^{Tcell-/-}$ mice treated with semaglutide showed a stronger induction in these pathways, perhaps attributable to an apparent lack of responses in some of the $Glp1r^{Tcell+/+}$ mice. Hence, the gut IEL GLP-1R appears dispensable for the metabolic benefits of GLP-1RAs but is required for selective effects of GLP-1RAs on the gut microbiota.

GLP-1RAs suppress T cell-mediated systemic inflammation, intestinal inflammation, and crypt cell death

Loss of the GLP-1R in gut IELs preserved endogenous L cell responsivity, glucose tolerance, and the metabolic responses to semaglutide. Accordingly, we next investigated whether the gut IEL GLP-1R contributes to gut mucosal integrity (Cheroutre et al., 2011). We examined the anti-inflammatory effects of GLP-1RAs in mice treated with an agonistic anti-CD3 antibody, an intervention shown to induce acute gut inflammation via gut T cell activation (Esplugues et al., 2011; Merger et al., 2002; Musch et al., 2002). We chose a dose of 35 μg anti-CD3 antibody for the *in vivo* experiments based on previous dose-response studies (Swamy et al., 2015). Clearly, 3 h after anti-CD3 treatment, plasma cytokine levels were markedly induced in wild-type C57BL/6J mice compared with mice treated with a dose- and isotype-matched antibody (Figure 3A). Plasma cytokine levels stayed elevated for at least 6 h and returned to almost basal levels by 24 h (data not shown). Notably, in mice treated with both anti-CD3 and the short-acting GLP-1RA exendin-4 for 3 h, the levels of multiple plasma cytokines were reduced by 30%–50%, except for interleukin-10 (IL-10) (Figure 3A).

Cytokine gene expression and cytokine protein content were upregulated in the jejunum of mice treated with anti-CD3 (Figures 3B and S3A). Exendin-4 downregulated expression of *Ifng*, but not *Tnf*, in the jejunum of anti-CD3-treated mice (Figure 3B). Although jejunal TNF-α content was increased in mice treated with anti-CD3 and exendin-4, content of other cytokines was not modulated by exendin-4 (Figure S3A). Activated gut IELs

release interferons in the gut epithelium, which in turn induce interferon-stimulated genes (ISGs) in the neighboring epithelial cells (Swamy et al., 2015). Anti-CD3 treatment induced expression of ISGs such as *Eif2ak2* and *Usp18* in the jejunum (Figure 3B); however, exendin-4 had no effect on jejunal ISG expression (Figure 3B).

To further localize gut cytokine and ISG expression, we sorted cells positive (gut IELs) and negative (mainly epithelial cells) for CD45 from the small intestinal epithelium of anti-CD3-treated mice, with or without exendin-4 administration. The expression of *Ifng* was almost exclusively within CD45+ gut IELs (Figure 3C), whereas levels of *Tnf* mRNA were higher in CD45− cells. The ISGs *Eif2ak2* and *Usp18* were highly enriched in CD45− epithelial cells and induced by anti-CD3 (Figure 3C). Interestingly, exendin-4 downregulated *Ifng,* but not *Tnf,* expression in CD45+ gut IELs from anti-CD3-treated mice, but it did not upregulate gut IEL levels of T cell-derived anti-inflammatory cytokine mRNAs such as *Il10* and *Il17a* (Figure S3B). Moreover, exendin-4 downregulated *Eif2ak2* and *Usp18* in gut epithelial CD45− cells from anti-CD3-treated mice (Figure 3C). In contrast to findings in the gut, the anti-inflammatory actions of exendin-4 were not detected in the liver of anti-CD3-treated mice (Figure S3C), an organ harboring a small population of GLP-1R+ γδT cells (McLean et al., 2021a).

Induction of IFN-γ, a primary effector cytokine of gut IELs, is causally linked to IEL cytotoxicity and epithelial cell death in the crypt compartment during gut inflammation (Bradford et al., 2017; Farin et al., 2014; Takashima et al., 2019). To quantify cell death events in the crypts of the small intestine, we analyzed histological sections from mice treated with anti-CD3 and semaglutide for 24 h. Semaglutide was used in the 24-h anti-CD3 experiments because of its longer half-life (Yu et al., 2018), which is more suitable for experiments with extended durations. Treatment with anti-CD3 increased cleaved caspase-3 (CC3)+ bodies per crypt in the small intestine (Figure 3D), with CC3 staining predominantly detected within the duodenum and jejunum. Semaglutide reduced the number of CC3+ bodies per crypt along the small bowel by at least 70% (Figure 3D). Collectively, these findings reveal that GLP-1R activation alleviates T cell-mediated inflammation evident by the reduction of plasma cytokine levels, downregulation of cytokine and ISG expression in the gut epithelium, and decreased CC3+ events in the crypt compartment.

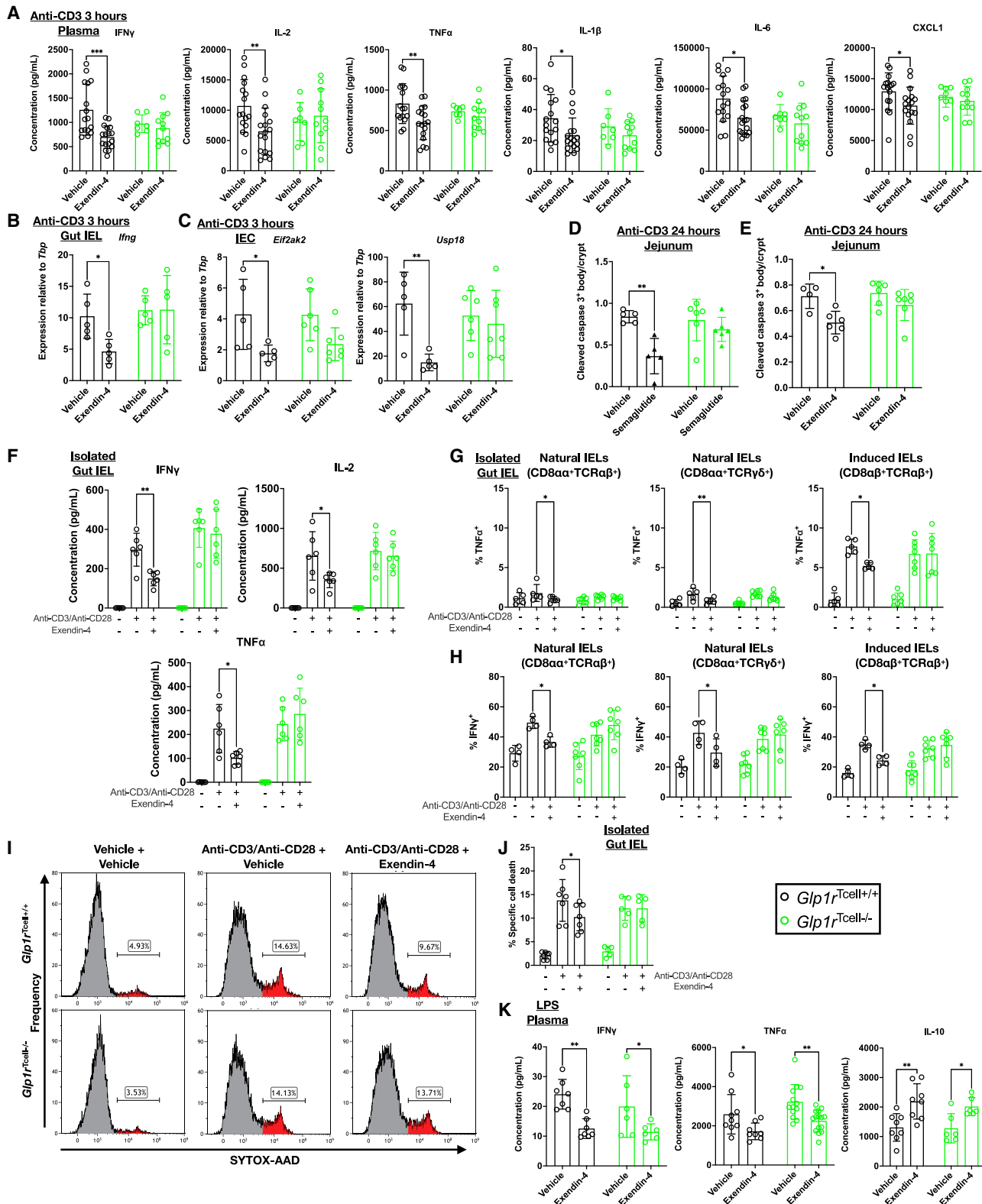## Activation of the GLP-1R suppresses the effector functions of gut IELs

To determine whether GLP-1RAs act directly on T cell GLP-1Rs to suppress T cell-mediated inflammation, we treated $Glp1r^{Tcell+/+}$ and $Glp1r^{Tcell-/-}$ mice with anti-CD3 and exendin-4 for 3 h. Plasma cytokine levels were similar in $Glp1r^{Tcell+/+}$ versus $Glp1r^{Tcell-/-}$ mice (Figure 4A). Exendin-4 lowered plasma levels of IFN-γ, IL-2,

(C) Expression of *Ifng*, *Tnf*, *Eif2ak2*, and *Usp18* in the epithelial cells (CD45−) and gut IELs (CD45+) sorted from C57BL/6J mice treated with anti-CD3 and exendin-4 (10 nmol/kg) for 3 h. n = 4–6.

(D) Top: representative images of cleaved caspase-3 staining by immunohistochemistry in the jejunum of C57BL/6J mice treated with anti-CD3 and semaglutide (10 μg/kg) for 24 h. Scale bar, 50 μm. Bottom: density of cleaved caspase-3-positive bodies in the duodenum, jejunum, and ileum of C57BL/6J mice treated with anti-CD3 and semaglutide (10 μg/kg) for 24 h. n = 4–7.

Data are represented as mean ± SD. * p < 0.05, ** p < 0.01, *** p < 0.001, and **** p < 0.0001. Two-way ANOVA tests were used in (A–C). Student's t tests were used in the bottom panel of (D).

Abbreviations: CC3, cleaved caspase-3.

Cell Metabolism
Article

CellPress

Figure 4. Activation of the GLP-1R suppresses the effector functions of gut IELs specifically

(A) Plasma cytokine levels in $Glp1r^{Tcell+/+}$ and $Glp1r^{Tcell-/-}$ mice treated with anti-CD3 and exendin-4 (10 nmol/kg) for 3 h. n = 7–17.

(B) Expression of $Ifng$ in gut IELs sorted from $Glp1r^{Tcell+/+}$ and $Glp1r^{Tcell-/-}$ mice treated with anti-CD3 and exendin-4 (10 nmol/kg) for 3 h. n = 5.

and TNF-α in anti-CD3-treated $Glp1r^{Tcell+/+}$ mice, but not in $Glp1r^{Tcell-/-}$ mice (Figure 4A). Similarly, exendin-4 reduced circulating levels of IL-1β, IL-6, and CXCL1 (Figure 4A), but not IL-10, IL-12 p70, IL-4, and IL-5 (Figure S4A), in $Glp1r^{Tcell+/+}$ mice. By contrast, these anti-inflammatory effects of exendin-4 were abolished in $Glp1r^{Tcell-/-}$ mice (Figure 4A). Levels of $Ifng$ in gut IELs, and $Eif2ak2$ and $Usp18$ in intestinal epithelial cells (IECs), were similar in anti-CD3-treated $Glp1r^{Tcell+/+}$ versus $Glp1r^{Tcell-/-}$ mice (Figures 4B and 4C). Exendin-4 downregulated expression of these genes in the gut IEL and IEC fractions isolated from $Glp1r^{Tcell+/+}$, but not from $Glp1r^{Tcell-/-}$, mice (Figures 4B and 4C). Jejunal cytokine content was similar across genotypes, irrespective of treatment with exendin-4; however, TNF-α content was elevated in exendin-4-treated $Glp1r^{Tcell+/+}$, but not in $Glp1r^{Tcell-/-}$, mice (Figure S4B).

In mice treated with anti-CD3, semaglutide reduced the frequency of CC3$^+$ bodies in the intestinal crypts of $Glp1r^{Tcell+/+}$, but not in $Glp1r^{Tcell-/-}$, mice (Figures 4D and S4C). Exendin-4, which has a shorter half-life than semaglutide, also reduced crypt cell death yet was slightly less effective than semaglutide in reducing the number of CC3$^+$ bodies in the jejunum of anti-CD3-treated $Glp1r^{Tcell+/+}$ mice, and the cytoprotective effect of exendin-4 on crypt cells was lost in anti-CD3-treated $Glp1r^{Tcell-/-}$ mice (Figure 4E). Semaglutide also reduced the frequency of TUNEL$^+$ bodies, another cell death marker, in the intestinal crypts of $Glp1r^{Tcell+/+}$, but not $Glp1r^{Tcell-/-}$, mice (Figures S4D and S4E). Furthermore, semaglutide downregulated $Ifng$—but not Tnf, $Eif2ak2$, or $Usp18$—in the jejunum of $Glp1r^{Tcell+/+}$ mice acutely treated with anti-CD3, an effect that was absent in $Glp1r^{Tcell-/-}$ mice (Figure S4F). Semaglutide also reduced IL-4 and IL-6—but not IFN-γ, IL-2, and TNF-α—jejunal cytokine content in $Glp1r^{Tcell+/+}$, but not in $Glp1r^{Tcell-/-}$, mice, treated with anti-CD3 for 24 h (Figure S4G). Taken together, deletion of the T cell GLP-1R eliminates the systemic and intestinal anti-inflammatory and cytoprotective actions of GLP-1RAs in the context of T cell-mediated inflammation.

We further assessed the anti-inflammatory effects of GLP-1RAs directly on gut IELs sorted from $Glp1r^{Tcell+/+}$ and $Glp1r^{Tcell-/-}$ mice using independent assays and inducers of T cell activation. First, we activated sorted gut IELs using plate-coated anti-CD3 or soluble phorbol 12-myristate-13-acetate (PMA)/ionomycin, the latter which activates T cells by activating protein kinase C (PKC) and mobilizing intracellular calcium while bypassing proximal TCR signaling events (Chatila et al., 1989). Direct IEL activation by either reagent stimulated IFN-γ, IL-2, and TNF-α secretion (Figures 4F and S4H). The extent of cytokine induction was similar across genotypes. Exendin-4 dampened the secretion of all three cytokines induced by anti-CD3 in gut IELs isolated from $Glp1r^{Tcell+/+}$, but not in IELs from $Glp1r^{Tcell-/-}$, mice (Figure 4F). By contrast, exendin-4 did not inhibit cytokine secretion in response to PMA/ionomycin in either genotype, thus revealing the dependence of anti-inflammatory effects of exendin-4 on proximal TCR signaling (Figure S4H). Anti-CD3 activation also stimulated IL-17A secretion from gut IELs; however, exendin-4 did not change IL-17A secretion in gut IELs from either $Glp1r^{Tcell+/+}$ or $Glp1r^{Tcell-/-}$ mice (Figure S4I). We next analyzed the actions of exendin-4 using isolated MLN and splenic cells. MLN cells secreted IFN-γ, IL-2, and TNF-α upon plate-bound anti-CD3 activation, but exendin-4 did not modulate cytokine levels in MLN cells (Figure S4J), or in splenocytes (data not shown), from either $Glp1r^{Tcell+/+}$ or $Glp1r^{Tcell-/-}$ mice.

We next examined the effects of GLP-1R activation on the effector functions of gut IELs, namely cytokine production and cytotoxicity. Intracellular cytokine staining of (1) CD8$\alpha\alpha^+$ TCR$\alpha\beta^+$ natural IELs; (2) CD8$\alpha\alpha^+$TCR$\gamma\delta^+$ natural IELs; and (3) CD8$\alpha\beta^+$TCR$\alpha\beta^+$ induced IELs, revealed enhanced TNF-α and IFN-γ production following anti-CD3 activation (Figures 4G and 4H), with greater augmentation of TNF-α production in induced IELs. Exendin-4 suppressed both TNF-α and IFN-γ production in all three types of gut IELs isolated from $Glp1r^{Tcell+/+}$ mice (Figures 4G and 4H). By contrast, these inhibitory effects of exendin-4 were lost in IELs from $Glp1r^{Tcell-/-}$ mice. We assessed the cytotoxicity of gut IELs by co-culturing activated gut IELs with carboxyfluorescein succinimidyl ester (CFSE)-labeled Jurkat cells, a cell type frequently deployed for assessing IEL cytotoxicity ex $vivo$ (Miura et al., 2005). The cytotoxicity of activated gut IELs was quantified by the percentage of CFSE$^+$ Jurkat cells positive for SYTOX-AAD, a nucleic acid stain that detects dead cells. Sorted gut IELs without anti-CD3 activation displayed modest cytotoxicity, whereas anti-CD3 activation increased the percentage of CFSE$^+$ SYTOX-AAD$^+$ cells (Figures 4I and 4J). Exendin-4 reduced the proportion of CFSE$^+$ SYTOX-AAD$^+$ Jurkat cells by 30% in wells co-cultured

(C) Expression of $Eif2ak2$ and $Usp18$ in epithelial cells isolated by EDTA stripping and TrypLE digestion from $Glp1r^{Tcell+/+}$ and $Glp1r^{Tcell-/-}$ mice treated with anti-CD3 and exendin-4 (10 nmol/kg) for 3 h. n = 5–7.

(D) Density of cleaved caspase-3-positive bodies as quantified by immunohistochemistry in the jejunum of $Glp1r^{Tcell+/+}$ and $Glp1r^{Tcell-/-}$ mice treated with anti-CD3 and semaglutide (10 μg/kg) for 24 h. n = 5 or 6.

(E) Density of cleaved caspase-3-positive bodies as quantified by immunohistochemistry in the jejunum of $Glp1r^{Tcell+/+}$ and $Glp1r^{Tcell-/-}$ mice treated with anti-CD3 and exendin-4 (10 nmol/kg) for 24 h. n = 4–7.

(F) Secreted cytokine levels from sorted $Glp1r^{Tcell+/+}$ and $Glp1r^{Tcell-/-}$ mouse gut IELs treated with plate-coated anti-CD3/anti-CD28 and exendin-4 (50 nM) for 5 h. n = 6.

(G and H) Intracellular staining of (G) TNF-α and (H) IFN-γ in sorted $Glp1r^{Tcell+/+}$ and $Glp1r^{Tcell-/-}$ mouse gut IELs treated with plate-coated anti-CD3/anti-CD28 and exendin-4 (50 nM) for 5 h. n = 4–7.

(I) Representative plots of cytotoxicity assays on sorted $Glp1r^{Tcell+/+}$ and $Glp1r^{Tcell-/-}$ mouse gut IELs treated with plate-coated anti-CD3/anti-CD28 and exendin-4 (50 nM) against Jurkat cells for 18 h. The red and gray area in the histograms denote populations gated for CFSE$^+$ SYTOX-AAD$^+$ and CFSE$^+$ SYTOX-AAD$^-$ cells, respectively.

(J) Cytotoxicity assays on sorted $Glp1r^{Tcell+/+}$ and $Glp1r^{Tcell-/-}$ mouse gut IELs treated with plate-coated anti-CD3/anti-CD28 and exendin-4 (50 nM) against Jurkat cells for 18 h. n = 5–7.

(K) Plasma cytokine levels in $Glp1r^{Tcell+/+}$ and $Glp1r^{Tcell-/-}$ mice treated with LPS and exendin-4 (10 nmol/kg) for 3 h. n = 6–15.

Data are represented as mean ± SD. * p < 0.05, ** p < 0.01, and *** p < 0.001. Two-way ANOVA tests were used in (A–H), (J), and (K).

Abbreviations: IEC, intestinal epithelial cell.

Cell Metabolism
Article

CellPress

with activated gut IELs from $Glp1r^{Tcell+/+}$ mice; however, these cytoprotective actions of exendin-4 were lost using gut IELs from $Glp1r^{Tcell-/-}$ mice (Figures 4I and 4J). Collectively, GLP-1RAs inhibit multiple effector functions of gut IELs in a GLP-1R-dependent manner.

We investigated other possible mechanisms that might explain the effect of GLP-1RAs on gut IEL-mediated inflammation. Because GLP-2, which is co-secreted with GLP-1, can suppress gut inflammation (Cani et al., 2009; Ivory et al., 2008; L'Heureux and Brubaker, 2003), we examined $Glp2r$ expression in the gut of $Glp1r^{Tcell+/+}$ and $Glp1r^{Tcell-/-}$ mice. Jejunal $Glp2r$ expression was similar in $Glp1r^{Tcell-/-}$ versus $Glp1r^{Tcell+/+}$ mice (Figure S4K). Unlike $Glp1r$, expression of $Glp2r$ was extremely low in isolated gut IELs relative to the jejunum. Together with the normal ileal GLP-2 content in $Glp1r^{Tcell-/-}$ mice (Figure 1Q), these data suggest that the GLP-2 system is unlikely to be involved in the anti-inflammatory effects of GLP-1RAs on gut IELs.

Considering gut immune cells outside of the epithelium could be targets of GLP-1RAs, we examined the expression of $Glp1r$ in the lamina propria. We purified CD3$^+$ T cells and CD11b$^+$ or CD11c$^+$ phagocytes from the lamina propria by FACS and quantified their $Glp1r$ expression. Interestingly, neither the lamina propria T cells nor the lamina propria phagocytes expressed appreciable levels of $Glp1r$ relative to whole jejunum or isolated gut IELs (Figure S4L). The identity of the sorted immune cells was confirmed by the expression of $Cd3g$ for T cells and $Cd68$ for phagocytes (Figure S4M). Hence, the effects of GLP-1RAs on gut T cell-mediated inflammation are unlikely to be mediated through direct actions on the lamina propria T cells and phagocytes.

These findings demonstrate that GLP-1RAs suppress T cell-mediated inflammation in gut IELs. We next assessed whether T cell GLP-1Rs are required for GLP-1RA-mediated inhibition of inflammation that arises independent of T cell activation, such as through lipopolysaccharide (LPS) administration (Rakipovski et al., 2018; Meng and Lowell, 1997). LPS produced comparable levels of plasma cytokines in $Glp1r^{Tcell+/+}$ versus $Glp1r^{Tcell-/-}$ mice (Figures 4K and S4N). In contrast with the robust gut IEL GLP-1R-dependent anti-inflammatory actions of exendin-4 in the context of anti-CD3 challenge, exendin-4 lowered plasma IFN-γ and TNF-α levels and raised IL-10 levels in both LPS-treated $Glp1r^{Tcell+/+}$ and $Glp1r^{Tcell-/-}$ mice (Figure 4K). Moreover, exendin-4 did not change circulating levels of IL-12, IL-1β, IL-2, IL-4, IL-5, IL-6, or CXCL1 in LPS-treated $Glp1r^{Tcell+/+}$ and $Glp1r^{Tcell-/-}$ mice (Figure S4N). Thus, GLP-1RAs effectively inhibit both T cell-induced and LPS-induced systemic inflammation, but GLP-1RAs act specifically on T cell GLP-1Rs to suppress T cell-induced rather than LPS-induced inflammation.

The gut IEL GLP-1R inhibits proximal TCR signaling in a PKA-dependent manner

To ascertain whether transcriptomic changes might underlie the suppression of IEL effector functions by GLP-1R activation, we performed bulk RNA sequencing (RNA-seq) experiments on IELs sorted from the small intestine of mice injected with anti-CD3 and exendin-4 for 3 h. Unexpectedly, only 25 genes were differentially expressed in vehicle-treated versus exendin-4-treated gut IELs (Figure S5A; Table S3). Downregulation of $Ifng$ by exendin-4 was consistent with prior findings (Figures 3C and 4B). We subjected the data to gene set enrichment analysis

for GO terms in biological function. Two terms of particular interest exhibited enrichment scores: one was in the NADH dehydrogenase complex assembly and the other in protein folding (Figure S5B). Both categories encompass the biology of T cell activation, which engenders increases in protein synthesis and metabolic switching (Geltink et al., 2018; Kemp and Poe, 2019). $Creld2$ and $Manf$, genes associated with protein folding, were downregulated with exendin-4 (Figure S5A). To validate these findings, we repeated these experiments using qPCR to assess gene expression in gut IELs. $Manf$, but not $Creld2$, was induced by T cell activation and downregulated by exendin-4 in gut IELs isolated from $Glp1r^{Tcell+/+}$ mice, with the downregulation of $Manf$ by exendin-4 abolished in gut IELs isolated from $Glp1r^{Tcell-/-}$ mice (Figure S5C). The totality of the RNA-seq data suggest that transcriptomic changes are not sufficient to explain the mechanisms linking GLP-1R signaling to inhibition of gut IEL activation.

Upon T cell activation by TCR ligation or CD3 cross-linking, CD3ζ chains are phosphorylated by lymphocyte-specific protein tyrosine kinase (Lck), an event that recruits and phosphorylates zeta chain of TCR-associated protein kinase 70 (ZAP70) (Vang et al., 2001). Activation of G protein-coupled receptors (GPCRs), such as the prostaglandin E2 receptor, suppresses T cell activation attributable to induction of cyclic adenosine monophosphate (cAMP), activation of PKA, and inhibition of proximal TCR signaling. We hypothesized that activation of the gut GLP-1R inhibits phosphorylation events in proximal TCR signaling to suppress gut IEL activation and effector functions.

To capture the rapid phosphorylation events in proximal TCR signaling (Mingueneau et al., 2014), we performed time course phosphorylation flow cytometry experiments. The phosphorylated proteins surveyed included the following: (1) cAMP-response element binding protein (CREB) at S133, which would be indicative of PKA and/or PKC activity in T cells (Hughes-Fulford et al., 2005), and is thought to drive PKA-dependent inhibition of T cell activation (Yao et al., 2013); (2) ZAP70 at Y319, an activating marker of ZAP70 phosphorylated by Lck (Williams et al., 1999); (3) SLP-76 at Y128, an activating marker of SLP-76 phosphorylated by ZAP70 (Bubeck Wardenburg et al., 1996); (4) extracellular signal-regulated kinase (ERK)1/2 at T202/Y204, which lies downstream of PKC activation (Franklin et al., 1994); and (5) Lck at Y319 and Y505, activating and inhibitory markers, respectively, that balance Lck activity for phosphorylating ZAP70, among others (Salmond et al., 2009).

The anti-CD3 activation induced phosphorylation of CREB S133, ZAP70 Y319, and SLP-76 Y128 (Figures 5A–5C). ERK1/2 pT202/T204 was mildly induced by anti-CD3 in CD8$\alpha\alpha^+$TCR$\alpha\beta^+$ and CD8$\alpha\alpha^+$TCR$\gamma\delta^+$ natural IELs, and such induction was stronger in CD8$\alpha\beta^+$TCR$\alpha\beta^+$-induced IELs (Figure S5D), a phenomenon that has been described (Brenes et al., 2021). Phosphorylation of Lck at Y394 and Y505 was unchanged in gut IELs following anti-CD3 activation (Figures S5E and S5F). Exendin-4 potentiated the induction of CREB pS133 in anti-CD3-activated CD8$\alpha\alpha^+$TCR$\alpha\beta^+$ and CD8$\alpha\alpha^+$TCR$\gamma\delta^+$ natural IELs (Figure 5A), consistent with the coupling of GLP-1R activation to raising intracellular cAMP, thereby promoting CREB S133 phosphorylation (Jhala et al., 2003; Yusta et al., 2015). Exendin-4 reduced the proportion of both natural and induced IELs positive for ZAP70 pY319 over the course of anti-CD3 activation (Figure 5B). Similarly, the
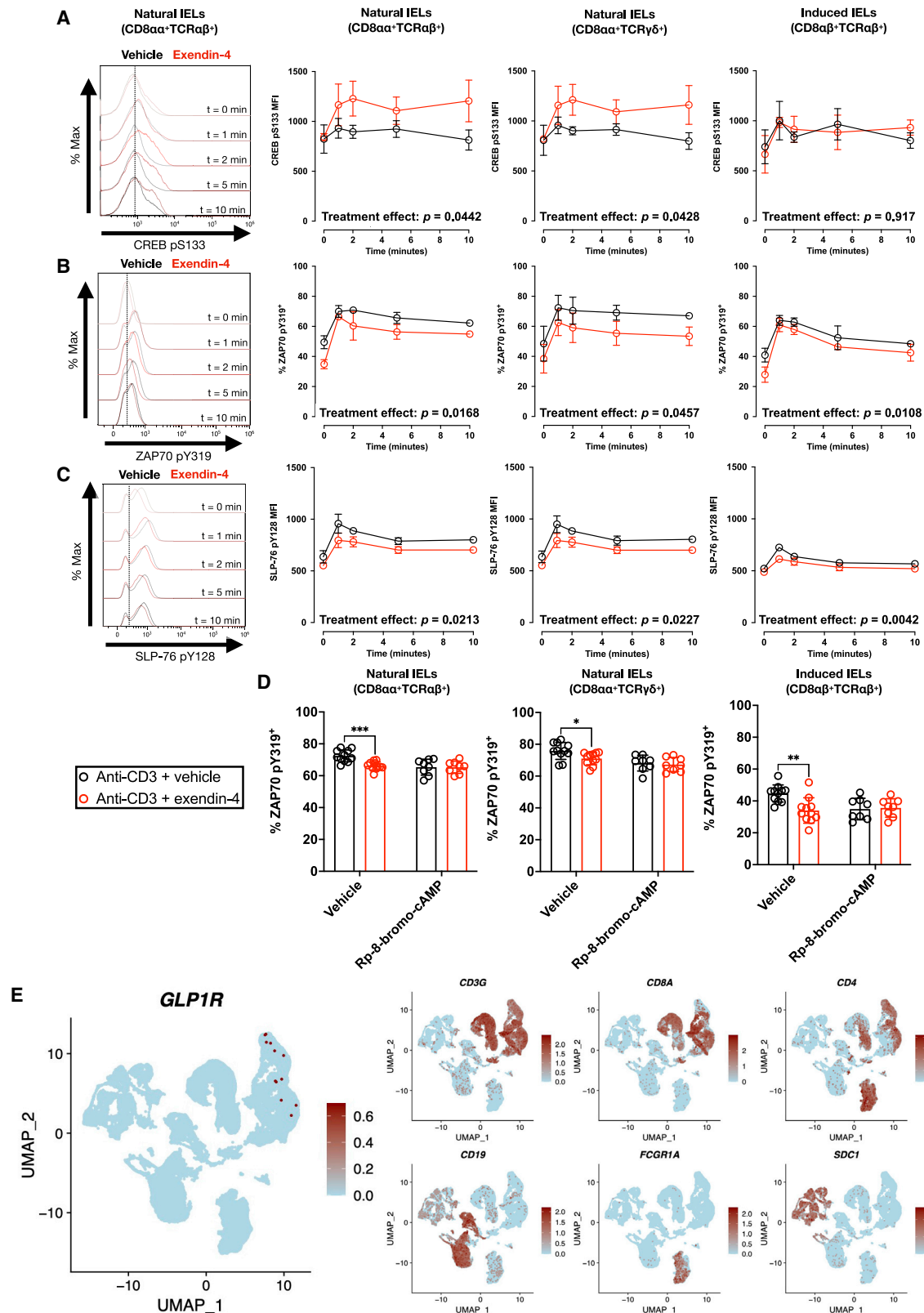
Figure 5. GLP-1R activation dampens gut IEL proximal TCR signaling in a PKA-dependent manner

(A, B, and C) Left panels: representative flow cytometric histograms for identifying phosphorylation targets in gut IELs. The dashed vertical lines in (A), (B), and (C) define the negative and positive populations. Right panels: time course plots showing flow cytometric analyses on the phosphorylation of (A) CREB S133, (B)

(legend continued on next page)

Cell Metabolism
Article

CellPress

fluorescence intensity of SLP-76 pY128 was decreased in both natural and induced IELs treated with anti-CD3 and exendin-4 (Figure 5C), and exendin-4 also lowered the proportion of the SLP-76 pY128$^+$ cells in the activated induced IELs (Figure S5G). These data reveal rapid inhibition of proximal TCR signaling by exendin-4 within minutes after T cell activation. ERK1/2 pT202/Y204, Lck pY394, and Lck pY505 were not affected by exendin-4 (Figures S5D–S5F). PMA/ionomycin activation did not increase ZAP70 pY319 or SLP-76 pY128 (Figures S5H and S5I), but it enhanced CREB pS133 and ERK1/2 pT202/Y204 (Figures S5J and S5K), both of which lie downstream of proximal TCR signaling. Consistently, exendin-4 did not modulate proximal TCR signaling in gut IELs activated by PMA/ionomycin (Figures S5D–S5G).

To ascertain the importance of cAMP and PKA as downstream mediators of exendin-4 action in IELs, we pretreated gut IELs with Rp-8-bromo-cAMP, a cAMP analog that antagonizes cAMP-dependent PKA activation, prior to exendin-4 treatment and anti-CD3 cross-linking. Exendin-4 lowered the percentage of ZAP70 pY319$^+$ cells in gut IELs pretreated with vehicle, actions abrogated by pretreatment with Rp-8-bromo-cAMP (Figure 5D).

Lastly, we explored the relevance of the GLP-1R in the human gut immune system. We analyzed single-cell RNA-seq (scRNA-seq) data generated as part of the gut cell atlas (Elmentaite et al., 2021). We retrieved data from more than 70,000 cells encompassing all major populations of gut immune cells, including T cells (CD3G$^+$), B cells (CD19$^+$), plasma cells (SDC1$^+$), and monocyte lineages (FCGR1A$^+$) (Figure 5E). We identified sporadic yet specific expression of GLP1R in human gut T cells. Expression of GLP1R occurred mostly in CD4$^+$ T cells, less so in CD8A$^+$ T cells, and was absent in B cells, plasma cells, and monocyte lineages (Figure 5E). Another independent scRNA-seq dataset that catalogs human immune cell transcriptomes also revealed sporadic GLP1R expression in gut T cells, but not in any other gut immune cells. (Domínguez Conde et al., 2022). These data extend the potential translational relevance of the GLP-1-IEL-sensing system to human gut T cells.

DISCUSSION

GLP-1RAs are increasingly utilized for the treatment of T2D and obesity (Drucker, 2022). These metabolic actions are reasonably well defined and involve signaling through GLP-1Rs in the islets and CNS, respectively (Drucker, 2022; Drucker et al., 2017; McLean et al., 2021b). Notably, studies of Itgb7 KO mice positioned the gut IEL GLP-1R as a sensor of GLP-1 bioavailability, providing signals to the L cell to modulate GLP-1 secretion (He et al., 2019). Here, we demonstrate that the gut IEL GLP-1R is not required for the control of glucose metabolism or body weight, but it functions as a key transducer of GLP-1R-dependent signals regulating a subset of the gut microbiota and T cell-driven inflammation.

Our current studies were prompted in part by results from Itgb7$^{-/-}$ mice linking loss of GLP-1R$^+$ gut IELs to control of GLP-1 bioavailability (He et al., 2019). These experiments used chimeric mice and bone marrow replacement strategies to invoke a role for the gut IEL GLP-1R in L cell communication. Here, we eliminated GLP-1R expression from gut IELs in two independent mouse lines, on two different genetic backgrounds. Although the Rag2$^{-/-}$;Il2rg$^{-/-}$ mice were on a BALB/c background, the metabolic phenotype of HFD-fed Rag2$^{-/-}$;Il2rg$^{-/-}$ mice recapitulated the improved glucose and insulin tolerance previously described for HFD-fed Itgb7$^{-/-}$ mice (He et al., 2019; Luck et al., 2015). Importantly, neither Rag2$^{-/-}$;Il2rg$^{-/-}$ mice nor Glp1r$^{Tcell-/-}$ mice on a C57BL/6J background, two mouse lines deficient in GLP-1R$^+$ gut IELs, showed enhanced circulating levels of GLP-1 before or after HFD feeding. Moreover, glucose tolerance and GLP-1 levels were not dysregulated in Tie2-Cre;Glp1r$^{fl/fl}$ mice also on a C57BL/6J background that lack GLP-1R expression in all hematopoietic and endothelial lineages including gut IELs (McLean et al., 2021a). Hence, while loss of gut T cells consistently improves glycemic control in mice with diet-induced obesity (Tsai et al., 2019), these metabolic phenotypes appear to be uncoupled from activity arising from loss of the gut IEL GLP-1R, based on our observations from three independent mouse lines lacking the gut IEL GLP-1R and showing no enhancement of circulating GLP-1 levels.

The epithelial localization of gut IELs, proximal to both gut microbiota and L cells (Bandeira et al., 1990; Zheng et al., 2020), renders the gut IEL GLP-1R well positioned to transduce immunomodulatory signals conveyed by GLP-1, via L cell sensing of microbial metabolites and cell wall products such as LPS (Heiss et al., 2021; Lebrun et al., 2017; Nguyen et al., 2014; Psichas et al., 2015). Indeed, whole body Glp1r$^{-/-}$ mice exhibit a dysregulated profile of gut microbiota and enhanced susceptibility to intestinal inflammation (Yusta et al., 2015). Chronic treatment with GLP-1RAs alters gut microbiota in mice (Kato et al., 2021; Madsen et al., 2019; Zhao et al., 2018), but interpretation of these changes is confounded by concomitant metabolic improvements and weight loss. Here, we show that semaglutide produced weight loss and microbial changes in both HFD-fed Glp1r$^{Tcell+/+}$ and Glp1r$^{Tcell-/-}$ mice, such as increased proportions of Enterococcus and Coriobacteriaceae UCG-002. By contrast, we detected microbial changes unique to the semaglutide-treated Glp1r$^{Tcell-/-}$ mice, such as increased representation of Mucispirillum and Parasutterella, in the absence of

ZAP70 Y319, and (C) SLP-76 Y128 in C57BL/6J mouse gut IELs activated with anti-CD3/anti-CD28 and exendin-4 (50 nM) for 5 min. n = 3 independent experiments.
(D) Flow cytometric analyses on the phosphorylation of ZAP70 Y319 in C57BL/6J mouse gut IELs treated with 300 μM Rp-8-bromo-cyclic AMP for 30 min, followed by exendin-4 (50 nM) for 5 min and anti-CD3 cross-linking for 5 min. n = 8–11.
(E) Published single-cell RNA-seq data on human gut immune cells showing GLP1R expression in human gut T cells. Markers used to define different gut immune cell populations include CD3G, CD8A, and CD4 (T cells); CD19 (B cells); FCGR1A (Fc gamma receptor Ia; monocyte lineages); and SDC1 (syndecan 1; plasma cells).
Data are represented as mean ± SD. * p < 0.05, ** p < 0.01, and *** p < 0.001. Two-way ANOVA tests were used in (A–C) and (D), and statistical significance was tested between exendin-4/anti-CD3-treated groups and vehicle/anti-CD3-treated groups.

perturbation to their gut IEL immunophenotypes. Furthermore, the functional abundance analysis reflects a pattern of increased *Escherichia coli* functions. Thus, selective loss of the gut IEL GLP-1R influences the interaction between GLP-1RAs, gut IELs, and gut microbiota. Nevertheless, these differences in microbiota did not impact the pharmacological actions of semaglutide on glucose homeostasis and body weight that were comparable in $Glp1r^{Tcell+/+}$ versus $Glp1r^{Tcell-/-}$ mice.

Absent overt anti-inflammatory effects of GLP-1RAs in HFD-fed mice, we used anti-CD3 to engage T cells *in vivo*, producing acute gut and systemic inflammation. The finding that exendin-4 acutely reduces levels of IFN-γ and TNF-α in the circulation and in gut IELs raises important considerations. Multiple lymphoid organs harboring mature T cells contribute IFN-γ to the circulation, challenging the ascertainment of the precise cellular origin of the increased cytokine production. However, representing the predominant site of T cell *Glp1r* expression (Heng et al., 2008; McLean et al., 2021a), gut IELs are strong candidates for conveying key signals among activated GLP-1R$^+$ cytotoxic T cells. Importantly, GLP-1RAs did not lower plasma cytokines in $Glp1r^{Tcell-/-}$ mice following anti-CD3 administration, further supporting activated gut IELs as key contributors to circulating cytokines in this context. We also detected the reduction of gut IEL-derived IFN-γ production and secretion following GLP-1RA administration. IFN-γ stimulates ISG expression in IECs (Swamy et al., 2015), thereby contributing directly and indirectly to intestinal crypt cell death (Chawla-Sarkar et al., 2003; Farin et al., 2014; Takashima et al., 2019). Thus, activation of GLP-1R blocks the pro-apoptotic cascade by reducing IEL IFN-γ secretion, leading to reduced ISG expression and epithelial cell death. In addition, suppression of systemic and gut inflammation by GLP-1RAs was observed in the context of direct inhibition of multiple gut IEL effector functions spanning cytokine production, cytokine secretion, and redirected cytotoxicity. The failure of GLP-1RAs to inhibit cytokine secretion from MLN cells or splenocytes further emphasizes the selective effects of GLP-1RAs on gut IELs relative to other T cell populations. These data suggest that the gut IEL GLP-1R represents a major target of GLP-1RAs in suppressing T cell-mediated inflammation and epithelial cell damage.

GLP-1RA-mediated reduction of TNF-α levels in the plasma and in anti-CD3-activated gut IELs likely facilitates protection of gut tissue from T cell-induced damage by preventing synergism of cytotoxicity between IFN-γ and TNF-α (Karki et al., 2021). In contrast to the gut IEL GLP-1R-dependent anti-inflammatory actions of GLP-1RAs in the setting of anti-CD3 administration, GLP-1RAs lowered plasma TNF-α in LPS-challenged $Glp1r^{Tcell-/-}$ mice. The preserved anti-inflammatory responses of GLP-1RAs in LPS-treated $Glp1r^{Tcell-/-}$ mice likely reflect the identity of the cells targeted by anti-CD3 versus LPS: anti-CD3 activates T cells, whereas LPS stimulates myeloid cells (Meng and Lowell, 1997). Hence, the precise context of the inflammatory stimulus serves as a critical determinant of the cell types and mechanisms through which GLP-1RAs reduce inflammation.

The use of flow cytometry helped delineate the effects of GLP-1RAs within individual gut IELs. GLP-1RAs reduced IFN-γ and TNF-α production and ZAP70 Y319 and SLP-76 Y128 phosphorylation in both natural and induced IELs. The dampening effects

of exendin-4 on the phosphorylation events during proximal TCR signaling were generally weaker on induced IELs than on natural IELs, which perhaps is attributable to the lower *Glp1r* expression within induced IELs relative to natural IELs. Nonetheless, reduction in both ZAP70 pY319 and its downstream target SLP-76 pY128 signifies dampened proximal TCR signaling and explains the impaired effector functions in GLP-1RA-treated gut IELs (Bubeck Wardenburg et al., 1996; Williams et al., 1999). The PKA-dependent inhibition of gut IEL proximal TCR signaling by GLP-1RAs resembles the mechanism by which prostaglandin E$_2$ acts on EP receptors to suppress T cell activation (Mustelin and Taskén, 2003). GLP-1R expression in T cells seems largely restricted to gut IELs, perhaps enabling GLP-1R signaling to selectively control gut IEL activity in response to local GLP-1 action within the gut epithelium.

The human and mouse gut IEL compartments exhibit numerous differences, including differences in the proportions of gut CD4$^+$ IELs (Mayassi and Jabri, 2018), the proportions of TCR$\gamma\delta^+$ IELs (Spencer et al., 1991), and IEL TCR$\gamma\delta$ clonotypes (Chowers et al., 1994; Takagaki et al., 1989). Yet, the IEL-L cell axis in humans and mice could be functionally similar. LPS-induced inflammation robustly stimulates L cell GLP-1 secretion in mice and humans (Lebrun et al., 2017). Furthermore, human subjects with gut inflammation linked to sepsis (Kahles et al., 2014), chemotherapy, or graft-versus-host disease (Ebbesen et al., 2019) represent conditions associated with higher levels of plasma GLP-1. With qPCR and reanalysis of published scRNA-seq data, we detected GLP-1R transcripts in both mouse and human gut T cells, and the expression of GLP-1R within the gut immune system appears restricted specifically to gut T cells. These observations posit L cell-derived GLP-1 as a hormone sensor of systemic and gut inflammation and a modulator of the effector functions of gut T cells in mice and perhaps in humans, likely transducing a subset of the anti-inflammatory effects evident following administration of GLP-1RAs.

Translational relevance of the current data
Our findings position the gut IEL GLP-1R as a key cellular node transducing actions of GLP-1RAs to modify gut microbiota and both local and systemic T cell-driven inflammation. T cell activation is central to the pathophysiology of atherosclerosis (Saigusa et al., 2020), NASH (Haas et al., 2019), and neurodegenerative disease (Dressman and Elyaman, 2022), clinical disorders that may be responsive to GLP-1RA therapy (Müller et al., 2019). GLP-1RAs have shown clear utility in treating T2D and obesity, while reducing rates of cardiovascular disease, cardiometabolic disorders that are characterized by dysregulated and enhanced inflammation. Furthermore, GLP-1RAs reduce hepatic and CNS inflammation (McLean et al., 2021a; Heiss et al., 2021) and are being investigated in NASH and neurodegenerative disorders (Cherney et al., 2021). Our data delineate the importance of gut T cell biology for the transduction of anti-inflammatory signals mediated by GLP-1Rs, findings with relevance for an emerging class of GLP-1R-dependent metabolic disease therapeutics.

Limitations of the study
We limited our metabolic studies of the gut IEL GLP-1R to chow-fed and HFD-fed mice, and it is possible the gut IEL GLP-1R may be important in non-dietary models of metabolic dysregulation.

Cell Metabolism
Article

CellPress

The effects of semaglutide on the gut microbiota of $Glp1r^{\text{Tcell}-/-}$ mice may be secondary to the metabolic benefits of semaglutide, such as weight loss. Alternative models to induce T cell activation, beyond the use of anti-CD3, could be utilized to probe gut IEL function *in vivo*. It is not clear why GLP-1RAs did not affect Lck pY394 and pY505, which would balance Lck activity to phosphorylate ZAP70, considering that activation of other GPCRs such as PGE$_2$ receptors enhances Lck pY505 through activation of C-terminal Src kinase (Csk) (Mustelin and Taskén, 2003). Dissection of phosphorylation events in gut IELs is hampered by the lack of Csk antibodies for flow cytometry, and the low protein yield from gut IEL isolation prevents the use of western blotting to detect these proteins. Moreover, the majority of our experiments were short term in nature, and the importance of T cell biology for the local and systemic anti-inflammatory actions of GLP-1RAs in sustained and chronic inflammation models requires evaluation.

STAR★METHODS

Detailed methods are provided in the online version of this paper and include the following:

- KEY RESOURCES TABLE
- RESOURCE AVAILABILITY
  - Lead contact
  - Material availability
  - Data and code availability
- EXPERIMENT MODELS AND SUBJECT DETAILS
  - Animal experiments
- METHOD DETAILS
  - Diet studies
  - Drug and chemical treatment
  - Glucose, lipid, and insulin tolerance tests
  - Metabolic cages
  - Gastric emptying tests
  - Portal vein blood collection
  - Analyte measurements
  - Gene expression analysis
  - 16s rRNA gene sequencing
  - Bulk RNA sequencing
  - Single-cell RNA sequencing analysis
  - Immunohistochemistry and immunofluorescence
  - Gut intraepithelial lymphocyte and epithelial cell isolation
  - Lamina propria immune cell isolation
  - Flow cytometry and fluorescence-activated cell sorting
  - *Ex vivo* T cell activation
  - Redirected cytotoxicity assays
  - Intracellular cytokine staining
  - Phosphorylation flow cytometry
- QUANTIFICATION AND STATISTICAL ANALYSIS

SUPPLEMENTAL INFORMATION

Supplemental information can be found online at https://doi.org/10.1016/j.cmet.2022.08.003.

AUTHOR CONTRIBUTIONS

B.A.M., C.K.W., L.L.B., B.Y., J.A.K., and D.M. designed and executed the experiments and reviewed and edited the manuscript. R.J.S. provided *Glp1r* floxed mice and edited the manuscript. D.J.D. designed the experiments, and both C.K.W. and D.J.D. wrote the manuscript.

REFERENCES

Athauda, D., Maclagan, K., Skene, S.S., Bajwa-Joseph, M., Letchford, D., Chowdhury, K., Hibbert, S., Budnik, N., Zampedri, L., Dickson, J., et al. (2017). Exenatide once weekly versus placebo in Parkinson's disease: a randomised, double-blind, placebo-controlled trial. Lancet *390*, 1664–1675.

Bandeira, A., Mota-Santos, T., Itohara, S., Degermann, S., Heusser, C., Tonegawa, S., and Coutinho, A. (1990). Localization of gamma/delta T cells to the intestinal epithelium is independent of normal microbial colonization. J. Exp. Med. *172*, 239–244.

Bankhead, P., Loughrey, M.B., Fernández, J.A., Dombrowski, Y., McArt, D.G., Dunne, P.D., McQuaid, S., Gray, R.T., Murray, L.J., Coleman, H.G., et al. (2017). QuPath: open source software for digital pathology image analysis. Sci. Rep. *7*, 16878.

Blighe, K., Rana, S., Turkes, E., Ostendorf, B., Grioni, A., and Lewis, M. (2021). Publication-ready volcano plots with enhanced colouring and labeling. (Bioconductor). https://github.com/kevinblighe/EnhancedVolcano.

Bolger, A.M., Lohse, M., and Usadel, B. (2014). Trimmomatic: a flexible trimmer for Illumina sequence data. Bioinformatics *30*, 2114–2120.

Bradford, E.M., Ryu, S.H., Singh, A.P., Lee, G., Goretsky, T., Sinh, P., Williams, D.B., Cloud, A.L., Gounaris, E., Patel, V., et al. (2017). Epithelial TNF receptor signaling promotes mucosal repair in inflammatory bowel disease. J. Immunol. *199*, 1886–1897.

Brenes, A.J., Vandereyken, M., James, O.J., Watt, H., Hukelmann, J., Spinelli, L., Dikovskaya, D., Lamond, A.I., and Swamy, M. (2021). Tissue environment, not ontogeny, defines murine intestinal intraepithelial T lymphocytes. eLife *10*, e70055.

Bubeck Wardenburg, J., Fu, C., Jackman, J.K., Flotow, H., Wilkinson, S.E., Williams, D.H., Johnson, R., Kong, G., Chan, A.C., and Findell, P.R. (1996). Phosphorylation of SLP-76 by the ZAP-70 protein-tyrosine kinase is required for T-cell receptor function. J. Biol. Chem. *271*, 19641–19644.

Callahan, B.J., McMurdie, P.J., Rosen, M.J., Han, A.W., Johnson, A.J., and Holmes, S.P. (2016). DADA2: high-resolution sample inference from Illumina amplicon data. Nat. Methods 13, 581–583.

Cani, P.D., Possemiers, S., Van de Wiele, T., Guiot, Y., Everard, A., Rottier, O., Geurts, L., Naslain, D., Neyrinck, A., Lambert, D.M., et al. (2009). Changes in gut microbiota control inflammation in obese mice through a mechanism involving GLP-2-driven improvement of gut permeability. Gut 58, 1091–1103.

Charpentier, J., Briand, F., Lelouvier, B., Servant, F., Azalbert, V., Puel, A., Christensen, J.E., Waget, A., Branchereau, M., Garret, C., et al. (2021). Liraglutide targets the gut microbiota and the intestinal immune system to regulate insulin secretion. Acta Diabetol. 58, 881–897.

Chatila, T., Silverman, L., Miller, R., and Geha, R. (1989). Mechanisms of T cell activation by the calcium ionophore ionomycin. J. Immunol. 143, 1283–1289.

Chaudhuri, A., Ghanim, H., Vora, M., Sia, C.L., Korzeniewski, K., Dhindsa, S., Makdissi, A., and Dandona, P. (2012). Exenatide exerts a potent antiinflammatory effect. J. Clin. Endocrinol. Metab. 97, 198–207.

Chawla-Sarkar, M., Lindner, D.J., Liu, Y.F., Williams, B.R., Sen, G.C., Silverman, R.H., and Borden, E.C. (2003). Apoptosis and interferons: role of interferon-stimulated genes as mediators of apoptosis. Apoptosis 8, 237–249.

Cherney, D.Z.I., Udell, J.A., and Drucker, D.J. (2021). Cardiorenal mechanisms of action of glucagon-like-peptide-1 receptor agonists and sodium-glucose cotransporter 2 inhibitors. Med (N Y) 2, 1203–1230.

Cheroutre, H., Lambolez, F., and Mucida, D. (2011). The light and dark sides of intestinal intraepithelial lymphocytes. Nat. Rev. Immunol. 11, 445–456.

Chimerel, C., Emery, E., Summers, D.K., Keyser, U., Gribble, F.M., and Reimann, F. (2014). Bacterial metabolite indole modulates incretin secretion from intestinal enteroendocrine L cells. Cell Rep. 9, 1202–1208.

Chowers, Y., Holtmeier, W., Harwood, J., Morzycka-Wroblewska, E., and Kagnoff, M.F. (1994). The V delta 1 T cell receptor repertoire in human small intestine and colon. J. Exp. Med. 180, 183–190.

Dobin, A., Davis, C.A., Schlesinger, F., Drenkow, J., Zaleski, C., Jha, S., Batut, P., Chaisson, M., and Gingeras, T.R. (2013). STAR: ultrafast universal RNA-seq aligner. Bioinformatics 29, 15–21.

Domínguez Conde, C., Xu, C., Jarvis, L.B., Rainbow, D.B., Wells, S.B., Gomes, T., Howlett, S.K., Suchanek, O., Polanski, K., King, H.W., et al. (2022). Cross-tissue immune cell analysis reveals tissue-specific features in humans. Science 376, eabl5197.

Douglas, G.M., Maffei, V.J., Zaneveld, J.R., Yurgel, S.N., Brown, J.R., Taylor, C.M., Huttenhower, C., and Langille, M.G.I. (2020). PICRUSt2 for prediction of metagenome functions. Nat. Biotechnol. 38, 685–688.

Dressman, D., and Elyaman, W. (2022). T cells: a growing universe of roles in neurodegenerative diseases. Neuroscientist 28, 335–348.

Drucker, D.J. (2018). Mechanisms of action and therapeutic application of glucagon-like peptide-1. Cell Metab. 27, 740–756.

Drucker, D.J. (2022). GLP-1 physiology informs the pharmacotherapy of obesity. Mol. Metab. 57, 101351.

Drucker, D.J., Habener, J.F., and Holst, J.J. (2017). Discovery, characterization, and clinical development of the glucagon-like peptides. J. Clin. Invest. 127, 4217–4227.

Ebbesen, M.S., Kissow, H., Hartmann, B., Grell, K., Gørløv, J.S., Kielsen, K., Holst, J.J., and Müller, K. (2019). Glucagon-like peptide-1 is a marker of systemic inflammation in patients treated with high-dose chemotherapy and autologous stem cell transplantation. Biol. Blood Marrow Transplant. 25, 1085–1091.

Elmentaite, R., Kumasaka, N., Roberts, K., Fleming, A., Dann, E., King, H.W., Kleshchevnikov, V., Dabrowska, M., Pritchard, S., Bolt, L., et al. (2021). Cells of the human intestinal tract mapped across space and time. Nature 597, 250–255.

Esplugues, E., Huber, S., Gagliani, N., Hauser, A.E., Town, T., Wan, Y.Y., O'Connor, W., Jr., Rongvaux, A., Van Rooijen, N., Haberman, A.M., et al. (2011). Control of TH17 cells occurs in the small intestine. Nature 475, 514–518.

Farin, H.F., Karthaus, W.R., Kujala, P., Rakhshandehroo, M., Schwank, G., Vries, R.G., Kalkhoven, E., Nieuwenhuis, E.E., and Clevers, H. (2014).

Paneth cell extrusion and release of antimicrobial products is directly controlled by immune cell-derived IFN-γ. J. Exp. Med. 211, 1393–1405.

Fiala, G.J., Schaffer, A.M., Merches, K., Morath, A., Swann, J., Herr, L.A., Hils, M., Esser, C., Minguet, S., and Schamel, W.W.A. (2019). Proximal Lck promotor-driven Cre function is limited in neonatal and ineffective in adult γδ T cell development. J. Immunol. 203, 569–579.

Flock, G., and Drucker, D.J. (2002). Pax-2 activates the proglucagon gene promoter but is not essential for proglucagon gene expression or development of proglucagon-producing cell lineages in the murine pancreas or intestine. Mol. Endocrinol. 16, 2349–2359.

Franklin, R.A., Tordai, A., Patel, H., Gardner, A.M., Johnson, G.L., and Gelfand, E.W. (1994). Ligation of the T cell receptor complex results in activation of the Ras/Raf-1/MEK/MAPK cascade in human T lymphocytes. J. Clin. Invest. 93, 2134–2140.

Geltink, R.I.K., Kyle, R.L., and Pearce, E.L. (2018). Unraveling the complex interplay Between T cell metabolism and function. Annu. Rev. Immunol. 36, 461–488.

Goodyear, A.W., Kumar, A., Dow, S., and Ryan, E.P. (2014). Optimization of murine small intestine leukocyte isolation for global immune phenotype analysis. J. Immunol. Methods 405, 97–108.

Grasset, E., Puel, A., Charpentier, J., Collet, X., Christensen, J.E., Tercé, F., and Burcelin, R. (2017). A specific gut microbiota dysbiosis of type 2 diabetic mice induces GLP-1 resistance through an enteric NO-dependent and gut-brain axis mechanism. Cell Metab. 25, 1075–1090.e5.

Gribble, F.M., and Reimann, F. (2016). Enteroendocrine cells: chemosensors in the intestinal epithelium. Annu. Rev. Physiol. 78, 277–299.

Haas, J.T., Vonghia, L., Mogilenko, D.A., Verrijken, A., Molendi-Coste, O., Fleury, S., Deprince, A., Nikitin, A., Woitrain, E., Ducrocq-Geoffroy, L., et al. (2019). Transcriptional network analysis implicates altered hepatic immune function in NASH development and resolution. Nat. Metab. 1, 604–614.

Hadjiyanni, I., Siminovitch, K.A., Danska, J.S., and Drucker, D.J. (2010). Glucagon-like peptide-1 receptor signalling selectively regulates murine lymphocyte proliferation and maintenance of peripheral regulatory T cells. Diabetologia 53, 730–740.

Hao, Y., Hao, S., Andersen-Nissen, E., Mauck, W.M., 3rd, Zheng, S., Butler, A., Lee, M.J., Wilk, A.J., Darby, C., Zager, M., et al. (2021). Integrated analysis of multimodal single-cell data. Cell 184, 3573–3587.e29.

He, S., Kahles, F., Rattik, S., Nairz, M., McAlpine, C.S., Anzai, A., Selgrade, D., Fenn, A.M., Chan, C.T., Mindur, J.E., et al. (2019). Gut intraepithelial T cells calibrate metabolism and accelerate cardiovascular disease. Nature 566, 115–119.

Heiss, C.N., Mannerås-Holm, L., Lee, Y.S., Serrano-Lobo, J., Håkansson Gladh, A., Seeley, R.J., Drucker, D.J., Bäckhed, F., and Olofsson, L.E. (2021). The gut microbiota regulates hypothalamic inflammation and leptin sensitivity in western diet-fed mice via a GLP-1R-dependent mechanism. Cell Rep. 35, 109163.

Helmstädter, J., Frenis, K., Filippou, K., Grill, A., Dib, M., Kalinovic, S., Pawelke, F., Kus, K., Kröller-Schön, S., Oelze, M., et al. (2020). Endothelial GLP-1 (glucagon-like peptide-1) receptor mediates cardiovascular protection by liraglutide in mice with experimental arterial hypertension. Arterioscler. Thromb. Vasc. Biol. 40, 145–158.

Heng, T.S., and Painter, M.W.; Immunological Genome Project Consortium (2008). The Immunological Genome Project: networks of gene expression in immune cells. Nat. Immunol. 9, 1091–1094.

Hennet, T., Hagen, F.K., Tabak, L.A., and Marth, J.D. (1995). T-cell-specific deletion of a polypeptide N-acetylgalactosaminyl-transferase gene by site-directed recombination. Proc. Natl. Acad. Sci. USA 92, 12070–12074.

Hughes-Fulford, M., Sugano, E., Schopper, T., Li, C.F., Boonyaratanakornkit, J.B., and Cogoli, A. (2005). Early immune response and regulation of IL-2 receptor subunits. Cell. Signal. 17, 1111–1124.

Hwang, I., Park, Y.J., Kim, Y.R., Kim, Y.N., Ka, S., Lee, H.Y., Seong, J.K., Seok, Y.J., and Kim, J.B. (2015). Alteration of gut microbiota by vancomycin and bacitracin improves insulin resistance via glucagon-like peptide 1 in diet-induced obesity. FASEB J. 29, 2397–2411.

Cell Metabolism
Article

CellPress

Imeryüz, N., Yeğen, B.C., Bozkurt, A., Coşkun, T., Villanueva-Peñacarrillo, M.L., and Ulusoy, N.B. (1997). Glucagon-like peptide-1 inhibits gastric emptying via vagal afferent-mediated central mechanisms. Am. J. Physiol. *273*, G920–G927.

Ivory, C.P., Wallace, L.E., McCafferty, D.M., and Sigalet, D.L. (2008). Interleukin-10-independent anti-inflammatory actions of glucagon-like peptide 2. Am. J. Physiol. Gastrointest. Liver Physiol. *295*, G1202–G1210.

James, O.J., Vandereyken, M., and Swamy, M. (2020). Isolation, characterization, and culture of intestinal intraepithelial lymphocytes. Methods Mol. Biol. *2121*, 141–152.

Jhala, U.S., Canettieri, G., Screaton, R.A., Kulkarni, R.N., Krajewski, S., Reed, J., Walker, J., Lin, X., White, M., and Montminy, M. (2003). cAMP promotes pancreatic beta-cell survival via CREB-mediated induction of IRS2. Genes Dev. *17*, 1575–1580.

Kahles, F., Meyer, C., Möllmann, J., Diebold, S., Findeisen, H.M., Lebherz, C., Trautwein, C., Koch, A., Tacke, F., Marx, N., and Lehrke, M. (2014). GLP-1 secretion is increased by inflammatory stimuli in an IL-6-dependent manner, leading to hyperinsulinemia and blood glucose lowering. Diabetes *63*, 3221–3229.

Karki, R., Sharma, B.R., Tuladhar, S., Williams, E.P., Zalduondo, L., Samir, P., Zheng, M., Sundaram, B., Banoth, B., Malireddi, R.K.S., et al. (2021). Synergism of TNF-alpha and IFN-gamma triggers inflammatory cell death, tissue damage, and mortality in SARS-CoV-2 infection and cytokine shock syndromes. Cell *184*, 149–168.e17.

Kato, S., Sato, T., Fujita, H., Kawatani, M., and Yamada, Y. (2021). Effects of GLP-1 receptor agonist on changes in the gut bacterium and the underlying mechanisms. Sci. Rep. *11*, 9167.

Kemp, K., and Poe, C. (2019). Stressed: the unfolded protein response in T cell development, activation, and function. Int. J. Mol. Sci. *20*, 1792.

Khan, S., Luck, H., Winer, S., and Winer, D.A. (2021). Emerging concepts in intestinal immune control of obesity-related metabolic disease. Nat. Commun. *12*, 2598.

Kim, E.R., Park, J.S., Kim, J.H., Oh, J.Y., Oh, I.J., Choi, D.H., Lee, Y.S., Park, I.S., Kim, S., Lee, D.H., et al. (2021). A GLP-1/GLP-2 receptor dual agonist to treat non-alcoholic steatohepatitis: targeting the gut-liver axis and microbiome. Hepatology *75*, 1523–1538.

Lebrun, L.J., Lenaerts, K., Kiers, D., Pais de Barros, J.P., Le Guern, N., Plesnik, J., Thomas, C., Bourgeois, T., Dejong, C.H.C., Kox, M., et al. (2017). Enteroendocrine L cells sense LPS after gut barrier injury to enhance GLP-1 secretion. Cell Rep. *21*, 1160–1168.

L'Heureux, M.C., and Brubaker, P.L. (2003). Glucagon-like peptide-2 and common therapeutics in a murine model of ulcerative colitis. J. Pharmacol. Exp. Ther. *306*, 347–354.

Love, M.I., Huber, W., and Anders, S. (2014). Moderated estimation of fold change and dispersion for RNA-seq data with DESeq2. Genome Biol. *15*, 550.

Luck, H., Tsai, S., Chung, J., Clemente-Casares, X., Ghazarian, M., Revelo, X.S., Lei, H., Luk, C.T., Shi, S.Y., Surendra, A., et al. (2015). Regulation of obesity-related insulin resistance with gut anti-inflammatory agents. Cell Metab. *21*, 527–542.

Madsen, M.S.A., Holm, J.B., Pallejà, A., Wismann, P., Fabricius, K., Rigbolt, K., Mikkelsen, M., Sommer, M., Jelsing, J., Nielsen, H.B., et al. (2019). Metabolic and gut microbiome changes following GLP-1 or dual GLP-1/GLP-2 receptor agonist treatment in diet-induced obese mice. Sci. Rep. *9*, 15582.

Manso, I., Torres, B., Andreu, J.M., Menéndez, M., Rivas, G., Alfonso, C., Díaz, E., García, J.L., and Galán, B. (2009). 3-Hydroxyphenylpropionate and phenylpropionate are synergistic activators of the MhpR transcriptional regulator from *Escherichia coli*. J. Biol. Chem. *284*, 21218–21228.

Martchenko, S.E., Martchenko, A., Cox, B.J., Naismith, K., Waller, A., Gurges, P., Sweeney, M.E., Philpott, D.J., and Brubaker, P.L. (2020). Circadian GLP-1 secretion in mice is dependent on the intestinal microbiome for maintenance of diurnal metabolic homeostasis. Diabetes *69*, 2589–2602.

Martin, M. (2011). Cutadapt removes adapter sequences from high-throughput sequencing reads. EMBnet J. *17*, 10–12.

Mayassi, T., and Jabri, B. (2018). Human intraepithelial lymphocytes. Mucosal Immunol. *11*, 1281–1289.

McLean, B.A., Wong, C.K., Campbell, J.E., Hodson, D.J., Trapp, S., and Drucker, D.J. (2021b). Revisiting the complexity of GLP-1 action from sites of synthesis to receptor activation. Endocr. Rev. *42*, 101–132.

McLean, B.A., Wong, C.K., Kaur, K.D., Seeley, R.J., and Drucker, D.J. (2021a). Differential importance of endothelial and hematopoietic cell GLP-1Rs for cardiometabolic versus hepatic actions of semaglutide. JCI Insight *6*, e153732.

McMurdie, P.J., and Holmes, S. (2013). phyloseq: an R package for reproducible interactive analysis and graphics of microbiome census data. PLoS One *8*, e61217.

Meng, F., and Lowell, C.A. (1997). Lipopolysaccharide (LPS)-induced macrophage activation and signal transduction in the absence of Src-family kinases Hck, Fgr, and Lyn. J. Exp. Med. *185*, 1661–1670.

Merger, M., Viney, J.L., Borojevic, R., Steele-Norwood, D., Zhou, P., Clark, D.A., Riddell, R., Maric, R., Podack, E.R., and Croitoru, K. (2002). Defining the roles of perforin, Fas/FasL, and tumour necrosis factor alpha in T cell induced mucosal damage in the mouse intestine. Gut *51*, 155–163.

Mingueneau, M., Krishnaswamy, S., Spitzer, M.H., Bendall, S.C., Stone, E.L., Hedrick, S.M., Pe'er, D., Mathis, D., Nolan, G.P., and Benoist, C. (2014). Single-cell mass cytometry of TCR signaling: amplification of small initial differences results in low ERK activation in NOD mice. Proc. Natl. Acad. Sci. USA *111*, 16466–16471.

Miura, N., Yamamoto, M., Fukutake, M., Ohtake, N., Iizuka, S., Ishige, A., Sasaki, H., Fukuda, K., Yamamoto, T., and Hayakawa, S. (2005). Anti-CD3 induces bi-phasic apoptosis in murine intestinal epithelial cells: possible involvement of the Fas/Fas ligand system in different T cell compartments. Int. Immunol. *17*, 513–522.

Montgomery, M.K., Hallahan, N.L., Brown, S.H., Liu, M., Mitchell, T.W., Cooney, G.J., and Turner, N. (2013). Mouse strain-dependent variation in obesity and glucose homeostasis in response to high-fat feeding. Diabetologia *56*, 1129–1139.

Müller, T.D., Finan, B., Bloom, S.R., D'Alessio, D., Drucker, D.J., Flatt, P.R., Fritsche, A., Gribble, F., Grill, H.J., Habener, J.F., et al. (2019). Glucagon-like peptide 1 (GLP-1). Mol. Metab. *30*, 72–130.

Musch, M.W., Clarke, L.L., Mamah, D., Gawenis, L.R., Zhang, Z., Ellsworth, W., Shalowitz, D., Mittal, N., Efthimiou, P., Alnadjim, Z., et al. (2002). T cell activation causes diarrhea by increasing intestinal permeability and inhibiting epithelial Na+/K+-ATPase. J. Clin. Invest. *110*, 1739–1747.

Mustelin, T., and Taskén, K. (2003). Positive and negative regulation of T-cell activation through kinases and phosphatases. Biochem. J. *371*, 15–27.

Newsome, P.N., Buchholtz, K., Cusi, K., Linder, M., Okanoue, T., Ratziu, V., Sanyal, A.J., Sejling, A.S., and Harrison, S.A.; NN9931-4296 Investigators (2021). A placebo-controlled trial of subcutaneous semaglutide in nonalcoholic steatohepatitis. N. Engl. J. Med. *384*, 1113–1124.

Nguyen, A.T., Mandard, S., Dray, C., Deckert, V., Valet, P., Besnard, P., Drucker, D.J., Lagrost, L., and Grober, J. (2014). Lipopolysaccharides-mediated increase in glucose-stimulated insulin secretion: involvement of the GLP-1 pathway. Diabetes *63*, 471–482.

Noyan-Ashraf, M.H., Shikatani, E.A., Schuiki, I., Mukovozov, I., Wu, J., Li, R.K., Volchuk, A., Robinson, L.A., Billia, F., Drucker, D.J., and Husain, M. (2013). A glucagon-like peptide-1 analog reverses the molecular pathology and cardiac dysfunction of a mouse model of obesity. Circulation *127*, 74–85.

Psichas, A., Reimann, F., and Gribble, F.M. (2015). Gut chemosensing mechanisms. J. Clin. Invest. *125*, 908–917.

Raetz, C.R., Reynolds, C.M., Trent, M.S., and Bishop, R.E. (2007). Lipid A modification systems in gram-negative bacteria. Annu. Rev. Biochem. *76*, 295–329.

Rakipovski, G., Rolin, B., Nøhr, J., Klewe, I., Frederiksen, K.S., Augustin, R., Hecksher-Sørensen, J., Ingvorsen, C., Polex-Wolf, J., and Knudsen, L.B. (2018). The GLP-1 analogs liraglutide and semaglutide reduce atherosclerosis in ApoE$^{-/-}$ and LDLr$^{-/-}$ mice by a mechanism that includes inflammatory pathways. JACC Basic Transl. Sci. *3*, 844–857.

Saigusa, R., Winkels, H., and Ley, K. (2020). T cell subsets and functions in atherosclerosis. Nat. Rev. Cardiol. 17, 387–401.

Salmond, R.J., Filby, A., Qureshi, I., Caserta, S., and Zamoyska, R. (2009). T-cell receptor proximal signaling via the Src-family kinases, Lck and Fyn, influences T-cell activation, differentiation, and tolerance. Immunol. Rev. 228, 9–22.

Sato, T., Shimizu, T., Fujita, H., Imai, Y., Drucker, D.J., Seino, Y., and Yamada, Y. (2020). GLP-1 receptor signaling differentially modifies the outcomes of sterile vs viral pulmonary inflammation in male mice. Endocrinology 161, bqaa201.

Sattar, N., Lee, M.M.Y., Kristensen, S.L., Branch, K.R.H., Del Prato, S., Khurmi, N.S., Lam, C.S.P., Lopes, R.D., McMurray, J.J.V., Pratley, R.E., et al. (2021). Cardiovascular, mortality, and kidney outcomes with GLP-1 receptor agonists in patients with type 2 diabetes: a systematic review and meta-analysis of randomised trials. Lancet Diabetes Endocrinol. 9, 653–662.

Segata, N., Izard, J., Waldron, L., Gevers, D., Miropolsky, L., Garrett, W.S., and Huttenhower, C. (2011). Metagenomic biomarker discovery and explanation. Genome Biol. 12, R60.

Sisley, S., Gutierrez-Aguilar, R., Scott, M., D'Alessio, D.A., Sandoval, D.A., and Seeley, R.J. (2014). Neuronal GLP1R mediates liraglutide's anorectic but not glucose-lowering effect. J. Clin. Invest. 124, 2456–2463.

Song, J., Willinger, T., Rongvaux, A., Eynon, E.E., Stevens, S., Manz, M.G., Flavell, R.A., and Galán, J.E. (2010). A mouse model for the human pathogen Salmonella typhi. Cell Host Microbe 8, 369–376.

Spencer, J., Isaacson, P.G., MacDonald, T.T., Thomas, A.J., and Walker-Smith, J.A. (1991). Gamma/delta T cells and the diagnosis of coeliac disease. Clin. Exp. Immunol. 85, 109–113.

Swamy, M., Abeler-Dörner, L., Chettle, J., Mahlakõiv, T., Goubau, D., Chakravarty, P., Ramsay, G., Reis e Sousa, C., Staeheli, P., Blacklaws, B.A., et al. (2015). Intestinal intraepithelial lymphocyte activation promotes innate antiviral resistance. Nat. Commun. 6, 7090.

Takagaki, Y., DeCloux, A., Bonneville, M., and Tonegawa, S. (1989). Diversity of gamma delta T-cell receptors on murine intestinal intra-epithelial lympho-cytes. Nature 339, 712–714.

Takashima, S., Martin, M.L., Jansen, S.A., Fu, Y., Bos, J., Chandra, D., O'Connor, M.H., Mertelsmann, A.M., Vinci, P., Kuttiyara, J., et al. (2019). T cell-derived interferon-gamma programs stem cell death in immune-mediated intestinal damage. Sci. Immunol. 4, eaay8556.

Tsai, S., Winer, S., and Winer, D.A. (2019). Gut T cells feast on GLP-1 to modulate cardiometabolic disease. Cell Metab. 29, 787–789.

Vang, T., Torgersen, K.M., Sundvold, V., Saxena, M., Levy, F.O., Skålhegg, B.S., Hansson, V., Mustelin, T., and Taskén, K. (2001). Activation of the COOH-terminal Src kinase (Csk) by cAMP-dependent protein kinase inhibits signaling through the T cell receptor. J. Exp. Med. 193, 497–507.

Varin, E.M., Mulvihill, E.E., Baggio, L.L., Koehler, J.A., Cao, X., Seeley, R.J., and Drucker, D.J. (2019). Distinct neural sites of GLP-1R expression mediate physiological versus pharmacological control of incretin action. Cell Rep. 27, 3371–3384.e3.

Wang, J., Vasaikar, S., Shi, Z., Greer, M., and Zhang, B. (2017). WebGestalt 2017: a more comprehensive, powerful, flexible and interactive gene set enrichment analysis toolkit. Nucleic Acids Res. 45, W130–W137.

Wang, V., Kuo, T.T., Huang, E.Y., Ma, K.H., Chou, Y.C., Fu, Z.Y., Lai, L.W., Jung, J., Choi, H.I., Choi, D.S., et al. (2021). Sustained release GLP-1 agonist PT320 delays disease progression in a mouse model of Parkinson's disease. ACS Pharmacol. Transl. Sci. 4, 858–869.

Wang, Z., Saha, S., Van Horn, S., Thomas, E., Traini, C., Sathe, G., Rajpal, D.K., and Brown, J.R. (2018). Gut microbiome differences between metformin- and liraglutide-treated T2DM subjects. Endocrinol. Diabetes Metab. 1, e00009.

Wichmann, A., Allahyar, A., Greiner, T.U., Plovier, H., Lundén, G.Ö., Larsson, T., Drucker, D.J., Delzenne, N.M., Cani, P.D., and Bäckhed, F. (2013). Microbial modulation of energy availability in the colon regulates intestinal transit. Cell Host Microbe 14, 582–590.

Williams, B.L., Irvin, B.J., Sutor, S.L., Chini, C.C., Yacyshyn, E., Bubeck Wardenburg, J., Dalton, M., Chan, A.C., and Abraham, R.T. (1999). Phosphorylation of Tyr319 in ZAP-70 is required for T-cell antigen receptor-dependent phospholipase C-gamma1 and Ras activation. EMBO J. 18, 1832–1844.

Yadav, H., Lee, J.H., Lloyd, J., Walter, P., and Rane, S.G. (2013). Beneficial metabolic effects of a probiotic via butyrate-induced GLP-1 hormone secretion. J. Biol. Chem. 288, 25088–25097.

Yao, C., Hirata, T., Soontrapa, K., Ma, X., Takemori, H., and Narumiya, S. (2013). Prostaglandin E_2 promotes Th1 differentiation via synergistic amplification of IL-12 signalling by cAMP and PI3-kinase. Nat. Commun. 4, 1685.

Yoon, H.S., Cho, C.H., Yun, M.S., Jang, S.J., You, H.J., Kim, J.H., Han, D., Cha, K.H., Moon, S.H., Lee, K., et al. (2021). Akkermansia muciniphila secretes a glucagon-like peptide-1-inducing protein that improves glucose homeosta-sis and ameliorates metabolic disease in mice. Nat. Microbiol. 6, 563–573.

Yu, M., Benjamin, M.M., Srinivasan, S., Morin, E.E., Shishatskaya, E.I., Schwendeman, S.P., and Schwendeman, A. (2018). Battle of GLP-1 delivery technologies. Adv. Drug Deliv. Rev. 130, 113–130.

Yusta, B., Baggio, L.L., Koehler, J., Holland, D., Cao, X., Pinnell, L.J., Johnson-Henry, K.C., Yeung, W., Surette, M.G., Bang, K.A., et al. (2015). GLP-1R ago-nists modulate enteric immune responses through the intestinal intraepithelial lymphocyte (IEL) GLP-1R. Diabetes 64, 2537–2549.

Zhao, L., Chen, Y., Xia, F., Abudukerimu, B., Zhang, W., Guo, Y., Wang, N., and Lu, Y. (2018). A glucagon-like peptide-1 receptor agonist lowers weight by modulating the structure of gut microbiota. Front. Endocrinol. (Lausanne) 9, 233.

Zheng, D., Liwinski, T., and Elinav, E. (2020). Interaction between microbiota and immunity in health and disease. Cell Res. 30, 492–506.

Cell Metabolism
Article

CellPress

STAR★METHODS

KEY RESOURCES TABLE

REAGENT or RESOURCE	SOURCE	IDENTIFIER
Antibodies		
Ultra-LEAF Purified Armenian Hamster IgG Isotype Control	BioLegend	CAT: 400959 RRID: AB_11203529
Ultra-LEAF Purified anti-mouse CD3ε Antibody	BioLegend	CAT: 100359 RRID: AB_2616673
Ultra-LEAF Purified anti-mouse CD28 Antibody	BioLegend	CAT: 102116 RRID: AB_11147170
Rabbit Anti-GLP-1 Sera	Developed in house (Flock and Drucker, 2002)	N/A
Rat Anti-CD3 Antibody	Abcam	CAT: ab11089 RRID: AB_2889189
Rabbit Anti-Cleaved Caspase-3 (Asp175) Antibody	Cell Signaling Technology	CAT: 9661 RRID: AB_2341188
Rat Anti-CD16/CD32 Antibody	BioLegend	CAT: 101301 RRID: AB_312800
Alexa Fluor 488 Anti-CD4 Antibody	BioLegend	CAT: 100425 RRID: AB_493520
PE Anti-CD8b Antibody	BioLegend	CAT: 126607 RRID: AB_961300
APC Anti-CD8a Antibody	BioLegend	CAT: 100711 RRID: AB_312750
APC/Cyanine7 Anti-CD3 Antibody	BioLegend	CAT: 100221 RRID: AB_2057374
Brilliant Violet 421 Anti-TCR β Antibody	BioLegend	CAT: 109229 RRID: AB_10933263
Brilliant Violet 510 Anti-TCR γ/δ Antibody	BioLegend	CAT: 118131 RRID: AB_2563534
Alexa Fluor 488 Anti-CD8a Antibody	BioLegend	CAT: 100726 RRID: AB_493423
PE/Cyanine7 Anti-TNF-α Antibody	BioLegend	CAT: 506323 RRID: AB_2204356
APC/Cyanine7 Anti-IFN-γ Antibody	BioLegend	CAT: 505849 RRID: AB_2616697
Alex Fluor 488 Anti-B220 Antibody	BioLegend	CAT: 103225 RRID: AB_389308
Alex Fluor 488 Anti-NK1.1 Antibody	BioLegend	CAT: 108718 RRID: AB_491383
PE/Cyanine7 Anti-CD45.2 Antibody	BioLegend	CAT: 109830 RRID: AB_1186098
APC/Cyanine7 Anti-CD11b Antibody	BioLegend	CAT: 101226 RRID: AB_830642
APC/Cyanine7 Anti-CD11c Antibody	BioLegend	CAT: 117324 RRID: AB_830649
Biotin Anti-CD3ε Antibody	BioLegend	CAT: 100303 RRID: AB_312668
Biotin Anti-CD28 Antibody	BioLegend	CAT: 102103 RRID: AB_312868
Alexa Fluor 488 Anti-ZAP70 (pY319)/SYK (pY352) Antibody	BD Biosciences	CAT: 557818 RRID: AB_396885

(Continued on next page)

Continued

REAGENT or RESOURCE	SOURCE	IDENTIFIER
PE Anti-CREB (pS133) Antibody	Cell Signaling Technology	CAT: 14228 RRID: AB_2798432
PE/Dazzle 594 Anti-ERK1/2 (pT202/Y204) Antibody	BioLegend	CAT: 369517 RRID: AB_2721689
PerCP/Cyanine5.5 Anti-CD8b Antibody	BioLegend	CAT: 126609 RRID: AB_961304
PE/Cyanine7 Anti-CD8a Antibody	BioLegend	CAT: 100721 RRID: AB_312760
Alexa Fluor 488 Anti-SLP76 (pY319)/SYK (pY352) Antibody	BD Biosciences	CAT: 558439 RRID: AB_647107
PE Anti-Lck (pY394) Antibody	BioLegend	CAT: 933103 RRID: AB_2820203
eFluor 660 Anti-Lck (pY505) Antibody	Thermo Fisher	CAT: 50-9076-42 RRID: AB_2574315
Chemicals, peptides, and recombinant proteins		
Exendin-4	Chi Scientific	Custom synthesis
Semaglutide (1.34 mg/mL pen)	Novo Nordisk	N/A
Lipopolysaccharides (LPS) from *Escherichia coli* O111:B4	MilliporeSigma	CAT: L2630-10MG
Humalog	Eli Lily	CAT: VL7510
Olive oil	MilliporeSigma	CAT: O1514
Acetaminophen	MilliporeSigma	CAT: A7085
DNase I from bovine pancreas	MilliporeSigma	CAT: D5025
Liberase TM	Roche	CAT: LIBTM-RO
Sitagliptin phosphate	MilliporeSigma	CAT: PHR1857-1G
RBC lysis buffer	BioLegend	CAT: 420301
RPMI 1640	Wisent Bioproducts	CAT: 350-000-EL
Fetal bovine serum	Wisent Bioproducts	CAT: 080-150
Penicillin-Streptomycin, 100x	Thermo Fisher	CAT: 15140148
HEPES, 1 M	Thermo Fisher	CAT: 15630106
TrypLE express enzyme (1X), no phenol red	Thermo Fisher	CAT: 12604013
SYTOX AADvanced dead cell stain kit (SYTOX-AAD)	Thermo Fisher	CAT: S10349
Sodium pyruvate, 100 mM	Thermo Fisher	CAT: 11360070
MEM non-essential amino acid, 100x	Thermo Fisher	CAT: 11140050
Cell Activation Cocktail without Brefeldin A (PMA/ionomycin)	BioLegend	CAT: 423301
CellTrace CFSE cell proliferation kit	Thermo Fisher	CAT: C34570
Brefeldin A	BioLegend	CAT: 420601
eBioscience Fixable Viability Dye eFluor 660	Thermo Fisher	CAT: 65-0864-14
Fixation/Permeabilization kit	BD Biosciences	CAT: 554714 RRID: AB_2869008
Streptavidin	BioLegend	CAT: 405150
Fixation Buffer	BD Biosciences	CAT: 554655 RRID: AB_2869005
Perm Buffer II	BD Biosciences	CAT: 558052 RRID: AB_2869119
Recombinant IL-15/IL-15R complex recombinant protein	Thermo Fisher	CAT: 14-8152-80
eBioscience Fixable Viability Dye eFluor 780	Thermo Fisher	CAT: 65-0865-14

Cell Metabolism
Article

CellPress

Continued

REAGENT or RESOURCE	SOURCE	IDENTIFIER
Rp-8-bromo-cyclic AMP	Cayman Chemical	CAT: 21584
Critical commercial assays		
V-Plex GLP-1 Total Kit	Mesoscale	CAT: K1503PD RRID: AB_2814818
V-Plex GLP-1 Active Kit	Mesoscale	CAT: K1503OD
Non-Esterified Fatty Acid assay reagents	Fujifilm Healthcare	CAT: 99934691, 99934791, 99934891, 99935191, 276-76491
Triglyceride tests for Cobas	Roche	CAT: 20767107322
V-Plex Proinflammatory Panel 1 Mouse Kit	Mesoscale	CAT: K15048D
In Situ Cell Death Detection Kit, Fluorescein	MilliporeSigma	CAT: 11684795910
ELISA MAX Deluxe Set Mouse IL-17A	BioLegend	CAT: 432504
Acetaminophen L3K assays	Sekisui	CAT: 506-10
Mouse GLP-2 ELISA	ALPCO	CAT: 48-GP2MS-E01
Deposited data		
16s rRNA-seq data for gut microbiota analysis in vehicle/semaglutide-treated HFD-fed $Glp1r^{Tcell+/+}$ and $Glp1r^{Tcell-/-}$ mice	This paper	GEO: GSE202452
Bulk RNA-seq data for gut IELs isolated from vehicle/exendin-4-treated C57BL/6J mice activated by anti-CD3	This paper	GEO: GSE202453
Raw and unprocessed data used for plotting the figures in this manuscript	This paper	Data S1
Experimental models: Cell lines		
Jurkat, Clone E6-1	ATCC, Jayne Danska	CAT: TIB-152 RRID: CVCL_0367
Experimental models: Organisms/strains		
Mouse: C;129S4-Rag2$^{tm1.1Flv}$ Il2rg$^{tm1.1Flv}$/J (Rag2$^{-/-}$; Il2rg$^{-/}$)	Jackson Laboratory	CAT: 014593 RRID: IMSR_JAX:014593
Mouse: C57BL/6J	Jackson Laboratory	CAT: 000664 RRID: IMSR_JAX:000664
Mouse: B6.Cg-Tg(Lck-cre)548Jxm/J (Lck-Cre)	Jackson Laboratory	CAT: 003802 RRID: IMSR_JAX:003802
Mouse: $Glp1r^{fl/fl}$	Randy Seeley	N/A
Oligonucleotides		
Ifng Taqman assays	Thermo Fisher	Mm01168134_m1
Tnf Taqman assays	Thermo Fisher	Mm00443258_m1
Eif2ak2 Taqman assays	Thermo Fisher	Mm01235643_m1
Usp18 Taqman assays	Thermo Fisher	Mm01188805_m1
Tbp Taqman assays	Thermo Fisher	Mm00446973_m1
Glp1r Taqman assays	Thermo Fisher	Mm00445292_m1
Creld2 Taqman assays	Thermo Fisher	Mm01309160_m1
Manf Taqman assays	Thermo Fisher	Mm00512511_m1
Glp2r Taqman assays	Thermo Fisher	Mm01329475_m1
Cd3g Taqman assays	Thermo Fisher	Mm00438095_m1
Cd68 Taqman assays	Thermo Fisher	Mm03047343_m1
Software and algorithms		
R 4.1.1	https://www.r-project.org/	N/A
Rstudio 1.4.1717	https://www.rstudio.com/	RRID: SCR_000432
Cutadapt 3.4	Martin, 2011	RRID: SCR_011841
Trimmomatic 0.39	Bolger et al., 2014	RRID: SCR_011848

(Continued on next page)

Continued

REAGENT or RESOURCE	SOURCE	IDENTIFIER
DADA2 1.20	Callahan et al., 2016	N/A
phyloseq 1.36.0	McMurdie and Holmes, 2013	RRID: SCR_013080
LEfSe	Segata et al., 2011	RRID: SCR_014609
PICRUSt2	Douglas et al., 2020	N/A
STAR 2.7.9a	Dobin et al., 2013	RRID: SCR_004463
DESeq2 1.32.0	Love et al., 2014	RRID: SCR_015687
EnhancedVolcano 1.10.0	Blighe et al., 2021 www.bioconductor.org	RRID: SCR_018931
QuPath 0.3.0	Bankhead et al., 2017	RRID: SCR_018257
WebGestalt 2017	Wang et al., 2017	RRID: SCR_006786
Seurat 4.1.0	Hao et al., 2021	RRID: SCR_007322
GraphPad Prism 9	GraphPad	RRID: SCR_002798
Kaluza 2.1	Beckman Coulter	RRID: SCR_016182
Other		
Teklad global 18% protein rodent diets (regular chow)	Envigo	CAT: 2018
Rodent diet with 60 kcal% fat (high-fat diet)	Research Diets	CAT: D12492i

RESOURCE AVAILABILITY

Lead contact
Daniel J Drucker (drucker@lunenfeld.ca) is the lead contact and takes full responsibility for the data in this paper.

Material availability
No unique reagents or materials were generated in these studies.

Data and code availability
No proprietary data or code is associated with this manuscript.

16s rRNA and Bulk RNA-seq data were deposited at gene expression omnibus (GEO) under the accession numbers GSE202452 and GSE202453, respectively. All unprocessed data used for plotting the figures and supplemental information in the manuscript are available as Data S1.

Any additional information required to reanalyze the data reported in this paper is available from the lead contact upon request.

EXPERIMENT MODELS AND SUBJECT DETAILS

Animal experiments
All animal procedures were approved by the Animal Care and Use Subcommittee at the Toronto Centre for Phenogenomics at Mount Sinai Hospital. Mice were housed up to five per cage in holding rooms on a twelve-hour light/dark cycle (7 am to 7 pm) at 23°C, with ad libitum access to water and regular chow with 18% kcal from fat (Envigo) or a HFD with 60% kcal from fat (Research Diets). All experiments were performed on genetic background-, sex-, age-, and littermate-matched animals. $Rag2^{-/-}$;$Il2rg^{-/-}$ mice, C57BL/6J mice, and *Lck*-Cre mice were purchased from Jackson Laboratory. Purchased $Rag2^{-/-}$; $Il2rg^{-/-}$ mice were on a BALB/c x 129S4 background, and they were backcrossed to a BALB/c background for at least eight generations prior to experiments.

$Glp1r^{fl/fl}$ mice (Sisley et al., 2014) were obtained from Randy Seeley and crossed with *Lck*-Cre mice to generate *Lck*-Cre; $Glp1r^{fl/fl}$ mice ($Glp1r^{Tcell-/-}$); both mouse lines were on a C57BL/6J background. *Lck*-Cre; $Glp1r^{+/+}$ (Cre-only control) mice and $Glp1r^{fl/fl}$ mice showed indiscernible differences in their phenotypes, and data from both genotypes were grouped together as the control group ($Glp1r^{Tcell+/+}$). All mice were group-housed as five mice per cage except for the $Glp1r^{Tcell-/-}$ mouse HFD studies. After performing the metabolic cage experiments on HFD-fed $Glp1r^{Tcell+/+}$ and $Glp1r^{Tcell-/-}$ mice, they stayed singly housed until the end of the study, which facilitated food intake measurement and fecal pellet collection during the semaglutide treatment HFD study.

METHOD DETAILS

Diet studies
Ten-week-old male $Rag2^{-/-}$;$Il2rg^{-/-}$ mice and $Glp1r^{Tcell-/-}$ mice with their respective littermate controls were placed on the HFD. Metabolic phenotyping was performed between eight and ten weeks after the diet commenced. HFD-fed $Rag2^{-/-}$; $Il2rg^{-/-}$ mice

Cell Metabolism
Article

CellPress

were euthanized at twelve weeks after the diet commenced. After 12 weeks of HFD feeding, $Glp1r^{Tcell+/+}$ and $Glp1r^{Tcell-/-}$ mice were randomly allocated into two groups and subcutaneously injected with vehicle (saline) or 10 μg/kg semaglutide daily for one week and euthanized thereafter.

Drug and chemical treatment

Exendin-4 (Chi Scientific) and semaglutide (Novo Nordisk Inc) were used in *in vivo* studies. For studies with exendin-4, mice were injected intraperitoneally (IP) with vehicle (saline) or 10 nmol/kg (41.8 μg/kg) exendin-4 at the same time as anti-CD3 or LPS injection. For experiments with semaglutide in the HFD studies, mice were injected subcutaneously with vehicle (saline) or 10 μg/kg (2.4 nmol/kg) semaglutide daily. For experiments with semaglutide in the anti-CD3 studies, mice were injected subcutaneously with vehicle (saline) or 10 μg/kg (2.4 nmol/kg) semaglutide immediately followed by anti-CD3 injection. For *in vivo* anti-CD3 challenges, mice were injected IP with 35 μg of Ultra-LEAF purified Armenian hamster IgG isotype control antibody (BioLegend) or Ultra-LEAF purified anti-mouse CD3ε antibody (BioLegend). For *in vivo* LPS challenges, mice were injected IP with 35 μg of LPS derived from *E. coli* O111:B4 (MilliporeSigma).

Glucose, lipid, and insulin tolerance tests

Mice were fasted for five hours prior to glucose or insulin tolerance tests, with the fast starting at 9 am. For oral and intraperitoneal glucose tolerance tests, mice were gavaged and injected IP, respectively, with a glucose bolus (2 g/kg of body weight). For lipid tolerance tests, mice were gavaged a fixed dose of 100 μL olive oil (MilliporeSigma). For insulin tolerance tests, mice were injected intraperitoneally with an insulin bolus (0.7 U/kg of body weight). Tail blood was collected into heparinized tubes at specified time points throughout the experiments and glucose levels were measured with a Contour handheld glucometer.

Metabolic cages

After ten weeks of HFD feeding, mice were placed in an EchoMRI machine to measure their fat and lean mass. For $Rag2^{-/-}$; $Il2rg^{-/-}$ mice, mice were placed in Columbus Laboratory Animal Monitoring System (Columbus Instruments) for measurement of metabolic parameters. For $Glp1r^{Tcell-/-}$ mice, animals were placed in Promethion High-Definition Behavioral Phenotyping System for Mice (Sable Systems) for measurement of metabolic parameters. Mice were allowed to acclimatize in the metabolic cages for 24 hours, and metabolic cage data were collected in the subsequent 48 hours. Food intake, water intake, energy expenditure, and locomotor activities were analyzed.

Gastric emptying tests

Mice were subjected to an acetaminophen absorption test to assess the rate of gastric emptying. Mice were fasted for 16 hours from 5 pm to 9 am. Fasted mice were then IP injected with vehicle (saline) or exendin-4, immediately followed by a gavage 1% (w/v) acetaminophen dissolved in water at a dose of 100 mg/kg of body weight. Tail blood samples were collected into heparinized tubes at 0, 15, 30, and 60 minutes after acetaminophen administration. Plasma acetaminophen levels were measured using an acetaminophen L3K assay (Sekisui).

Portal vein blood collection

Active GLP-1 levels in portal vein blood in response to glucose were measured as described (Grasset et al., 2017). Mice were fasted for 5 hours starting at 9 am. Fasted mice were gavaged with the dipeptidyl peptidase-IV inhibitor sitagliptin (400 μg/mouse). Thirty minutes after sitagliptin, mice were gavaged with vehicle (water) or a glucose solution (2 g/kg) and then immediately anaesthetized with an IP injection of Avertin (200 μg/kg). Ten minutes later, the mice were dissected to access the portal vein and a beveled capillary tube was inserted into the portal vein. A 200 μL volume of portal vein blood was collected for active GLP-1 measurement.

Analyte measurements

All plasma samples were prepared by mixing nine parts of blood with one part of TED (5000 KIU/mL Trasylol, 4 mM EDTA, 0.1 nM diprotin A) on ice followed by spinning at 13000 x g for five minutes. Tissue lysates for protein measurement were prepared by homogenizing tissue pieces in a homogenization buffer (50 mM Tris at pH 8, 1 mM EDTA, 10% glycerol (w/v), 0.067% Brij-35 (w/v)) supplemented with protease inhibitors (MilliporeSigma) using the TissueLyser II (QIAgen). Insulin, total GLP-1, active GLP-1, IFNγ, IL-10, IL-12 p70, IL-1β, IL-2, IL-4, IL-5, IL-6, CXCL1, TNFα, IL-17A, triglyceride, and non-esterified fatty acid were measured in the plasma or tissue lysate by ELISAs or colourimetric assays as per manufacturer's instructions.

Gene expression analysis

PBMCs were isolated by subjecting whole blood to RBC lysis using RBC lysis buffer (Biolegend). Total RNA was extracted by homogenizing tissues in TRIzol using the TissueLyser II, followed by standard RNA precipitation with ethanol. Single strand cDNA was synthesized using Superscript III (Thermo Fisher) and random primers. Quantitative PCR was set up in 384-well plates with TaqMan Fast Advanced Master Mix (Thermo Fisher) and Taqman probes, and the plates were run on a QuantStudio 5 system (Thermo Fisher). Relative expression was calculated by the $2^{-\Delta\Delta CT}$ method using *Tbp* as the reference gene.

16s rRNA gene sequencing

Fecal samples were collected from the distal end of the colon and snap frozen in liquid nitrogen prior to genomic DNA extraction and 16s rRNA gene sequencing as described previously (Yusta et al., 2015). Primers targeting V3-V4 regions were used to generate amplicons for barcoded sequencing library preparation. The 16s rRNA sequencing libraries were run on a MiSeq (Illumina) with a read length of 2 x 300 bp. Raw reads were adaptor-trimmed, followed by quality control and taxonomy assignment in DADA2 (Callahan et al., 2016). Downstream analysis was performed in phyloseq (McMurdie and Holmes, 2013). Differential abundance analyses were performed using DESeq2 and LEfSE (Love et al., 2014; Segata et al., 2011). Functional abundance analyses were performed using PICRUSt2 (Douglas et al., 2020).

Bulk RNA sequencing

Total RNA isolated from sorted gut IELs was prepared into stranded mRNA library using TruSeq stranded mRNA library preparation kit (Illumina) and sequenced on a NovaSeq (Illumina) with a read length of 2 x 200 bp. An average of 25 million paired-end reads was obtained per library. Sequencing reads were aligned to mm10 using STAR (Dobin et al., 2013) and a count table was generated for downstream DESeq2 analysis (Love et al., 2014). Differentially expressed genes were defined as adjusted p value < 0.05. Volcano plots were generated using the EnhancedVolcano package (Blighe et al., 2021) and gene set enrichment analysis was performed on Webgestalt (Wang et al., 2017).

Single-cell RNA sequencing analysis

Published single-cell RNA-sequencing data of the human gut cell atlas were reanalyzed for examining the expression of *GLP1R* in human gut T cells (Elmentaite et al., 2021). The count matrices for all gut immune cells available were reaggregated and UMAP plots were generated with a standard pipeline and default parameters using Seurat 4.1.0 (Hao et al., 2021).

Immunohistochemistry and immunofluorescence

Tissues were fixed in 10% neutral buffered formalin at room temperature for 24 hours, followed by processing and embedding in paraffin blocks. Sections with a thickness of 4 μm were obtained for immunohistochemistry. Immunohistochemistry was performed with a Bond-RX Fully Automated IHC Stainer (Leica Biosystems) using the following antibodies: anti-GLP-1 (1/5000), anti-CD3 (1/150; Abcam), and anti-cleaved caspase-3 (1/400; Cell Signaling Technology). TUNEL staining was performed using In Situ Cell Death Detection Kit, Fluorescein per manufacturer's instructions (MilliporeSigma). Stained slides were scanned on a Nanozoomer (Hamamatsu) at 20x magnification and positive cells were counted using QuPath in a blinded manner (Bankhead et al., 2017).

Gut intraepithelial lymphocyte and epithelial cell isolation

Gut IELs were isolated from the small intestine as previously described (James et al., 2020). The small intestine was cut into 0.5-cm pieces and shaken in a complete RPMI 1640 medium (supplemented with 10% fetal bovine serum, 1/100 penicillin/streptomycin, and 1 mM HEPES) with 1 mM DTT at 37°C for 20 minutes. The supernatant was spun down and discarded and the tissue pieces were vortexed in fresh complete RPMI 1640. The subsequent supernatant was spun down to pellet the cells, resuspended in 36% Percoll, and laid upon a 67% Percoll layer. The Percoll gradient was spun at 700 x g for 20 minutes with no acceleration or brake. The interphase was recovered and washed, and the resulting cell pellet was subject to flow cytometry or further purification by fluorescence-activated cell sorting (FACS) prior to functional assays. For gene expression analysis of the epithelial cells in Figure 3, the small intestine pieces were processed identically as above except the Percoll steps were omitted. The cells were subjected to FACS, and intestinal epithelial cells were sorted as CD45⁻. For gene expression analysis of the epithelial cells in Figure 4, the epithelium was stripped in 2 mM EDTA in HBSS without calcium or magnesium at 4°C for 30 minutes followed by incubation at 37°C for 20 minutes. The stripped epithelium was digested into single cells using 1x TrypLE (Thermo Fisher) at 37°C for five minutes. The epithelial single cell suspension was lyzed in TRIzol for RNA processing.

Lamina propria immune cell isolation

Lamina propria cells were isolated based on a published protocol (Goodyear et al., 2014). The small intestine was cleaned, cut into 0.5-cm pieces, and incubated in 5 mM EDTA, 5 mM DTT, and 2% v/v FBS in HBSS without calcium or magnesium at 37°C for 15 minutes to remove the epithelium. The gut tissue pieces were vortexed briefly and the supernatant was discarded. The EDTA washes were repeated for a total of four washes. The tissues were then minced and transferred into HBSS. DNase I (200 KU/mL; MilliporeSigma) and Liberase TM (0.2 Wünsch U/mL; Roche) were added to the minced tissues and the tissues were incubated at 37°C for 30 minutes. The tissues were gently triturated into single cell suspensions and subjected to a 67%/36% Percoll gradient identical to that of IEL isolation. Enriched lamina propria immune cells were then processed for FACS.

Flow cytometry and fluorescence-activated cell sorting

For flow cytometry, cells were blocked with anti-CD16/CD32 prior to staining. For identification of gut IEL subpopulations, blocked cells in 100 μL of buffer were stained with surface marker antibodies against the following antigens (BioLegend): CD4 (0.05 μg), CD8b (0.2 μg), CD8a (0.3 μg), CD3 (0.4 μg), TCR β (0.4 μg), and TCR γ/δ (0.3 μg), together with their corresponding compensation and staining controls. Flow analysis was performed on a Gallios flow cytometer (Beckman Coulter). Sorting of the gut IEL subpopulations was performed on a MoFlo Astrios cell sorter (Beckman Coulter). For enrichment of gut IELs for downstream T cell assays, Percoll-purified

Cell Metabolism
Article

CellPress

gut IELs were sorted by forward/side scatter properties and absence of SYTOX-AAD on a MA900 cell sorter (Sony). Gut IELs purified by FACS were confirmed by flow cytometry as more than 90% CD3$^+$. For sorting of lamina propria T cells and phagocytes, Percoll-purified lamina propria immune cells were stained with CD45.2 (0.3 μg), B220 (2 μg), NK1.1 (0.25 μg), CD3 (0.3 μg), CD11b (0.3 μg), CD11c (0.3 μg), and SYTOX-AAD. Lamina propria T cells were sorted and defined as live/CD45$^+$/NK1.1$^-$/B220$^-$/CD11b$^-$/CD11c$^-$/CD3$^+$, and lamina propria phagocytes were sorted and defined as live/CD45$^+$/NK1.1$^-$/B220$^-$/CD3$^-$/CD11b$^+$ or CD11c$^+$.

Ex vivo T cell activation
Sorted gut IELs were allowed to rest in complete RPMI 1640, supplemented with 1 mM sodium pyruvate and 1x non-essential amino acids, in a tissue culture incubator at 37°C, 5% CO$_2$ for 30 minutes before activation. Rested cells (500,000 cells/well; 2 x 10^6 cell/mL) were plated in a 24-well plate coated with 5 μg/mL Ultra-LEAF purified anti-mouse CD3ϵ (BioLegend) and 1 μg/mL Ultra-LEAF purified anti-mouse CD28 or the isotype control, and with or without 50 nM exendin-4. PMA/ionomycin activation was performed by adding Cell Activation Cocktail without Brefeldin A (1/500; BioLegend) to the cells. Cells were activated for five hours, and the supernatant was recovered for cytokine quantification.

Redirected cytotoxicity assays
To prepare target cells for testing the cytotoxicity of gut IELs, Jurkat cells (ATCC) were labeled with 300 nM carboxyfluorescein succinimidyl ester (CFSE) at 37°C for 20 minutes. In each well, 10,000 CFSE-labelled Jurkat cells were incubated with 200,000 sorted gut IELs (20:1 effector-to-target ratio) in anti-CD3- or isotype control- coated wells for 19 hours to induce redirected cytotoxicity, with or without the presence of 50 nM exendin-4. Recombinant IL-15/IL-15R complex recombinant protein (Thermo Fisher) was added to enhance the viability of gut IELs cultured overnight (James et al., 2020). Samples were then stained with SYTOX-AAD and analyzed on the Gallios flow cytometer.

Intracellular cytokine staining
Rested gut IELs were activated by plate-bound anti-CD3/anti-CD28 in the presence of 5 μg/mL Brefeldin A (BioLegend). A fixable viability dye eFluor 660 (1/1000) was added at the last ten minutes of the activation. Cells were recovered after five hours of activation and fixed and permeabilized using a Fixation/Permeabilization kit (BD Biosciences). Staining was performed using antibodies against CD8a (0.25 μg), CD8b (0.2 μg), TNFα (0.25 μg), IFNγ (0.1 μg), TCR β (0.4 μg), and TCR γ/δ (0.3 μg). Samples were then analyzed on the Gallios flow cytometer.

Phosphorylation flow cytometry
Rested gut IELs were activated using a crosslinking protocol for studying the acute changes in T cell signaling (Mingueneau et al., 2014). Gut IELs were treated with or without 50 nM exendin-4 for five minutes prior to CD3 crosslinking. A fixable viability dye eFluor 780 (1/1000) was added at the same time. Soluble 5 μg/mL biotin anti-CD3 and 1 μg/mL biotin anti-CD28 were then added to the cells at 37°C for 2 minutes. To crosslink the cells, 24 μg/mL streptavidin was added to the cells for different durations. For PMA/ionomycin activation, cells were treated with Cell Activation Cocktail without Brefeldin A (BioLegend) for 10 minutes after the exendin-4 pretreatment. Activation was quenched by adding Fixation Buffer (BD Biosciences) to the wells in 1:1 ratio for 10 minutes. Cells were permeabilized using Perm Buffer II (BD Biosciences) and stained with antibodies against the following antigens: ZAP70 pY319 (20 μL), CREB pS133 (2 μL), ERK1/2 pT202/Y204 (5 μL), SLP76 pY128 (20 μL), Lck pY394 (5 μL), Lck pY505 (5 μL), CD8b (0.12 μg), CD8a (0.3 μg), TCR β (0.4 μg), and TCR γ/δ (0.3 μg). In Rp-8-bromo-cyclic AMP experiments, rested gut IELs were treated with 300 μM Rp-8-bromo-cyclic AMP (dissolved in RPMI) or vehicle (RPMI) for 30 minutes, followed by treatment with exendin-4 and anti-CD3 crosslinking. Samples were then analyzed on the Gallios flow cytometer. The percentages of cells positive for a given phospho-antigen were reported whenever possible. For SLP-76 pY128, both the percentage of cells positive for SLP-76 pY128 and the median fluorescence intensity (MFI) of the said population were reported. For CREB pS133, MFI was reported because the signals did not follow a binomial distribution.

QUANTIFICATION AND STATISTICAL ANALYSIS

Data are expressed as the mean ± SD. Student's t-tests, one-way ANOVA tests with Dunnet post-hoc tests, and two-way or repeated-measures ANOVA tests with Sidak post-hoc tests were used to calculate statistical significance as appropriate in GraphPad Prism 9 (GraphPad). For repeated-measures ANOVA, the main treatment or genotype effects were tested unless otherwise specified and the p values were reported within the corresponding panels. A p value less than 0.05 was deemed statistically significant.
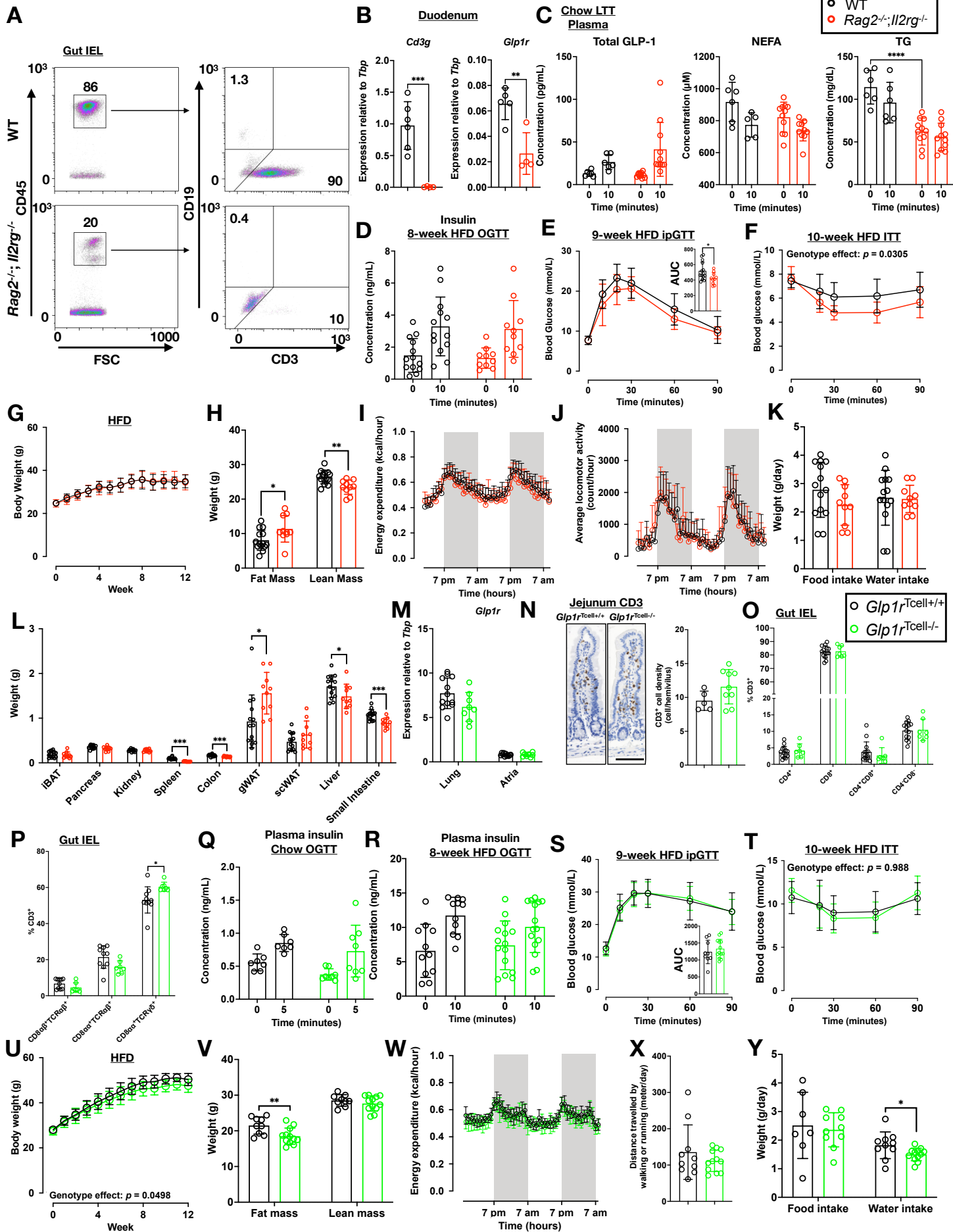
Figure S1, related to Figure 1. Metabolic phenotyping of chow-fed and HFD-fed *Rag2*^{-/-}; *Il2rg*^{-/-} mice and *Glp1r*[Tcell-/-] mice.

(A) Representative plots for flow cytometric analyses of WT and *Rag2*^{-/-}; *Il2rg*^{-/-} mouse IELs. n=3.

(B) Expression of *Cd3g* and *Glp1r* in WT and *Rag2*^{-/-};*Il2rg*^{-/-} mouse duodena. n=4-5.

(C) Plasma total GLP-1 levels (left panel), plasma NEFA levels (middle panel), and plasma TG levels (right panel) of WT and *Rag2*^{-/-}; *Il2rg*^{-/-} mice after a five-hour fast followed by gavaging with a bolus of olive oil (100 μL/mouse). n=6-11.

(D) Plasma insulin levels of WT and *Rag2*^{-/-}; *Il2rg*^{-/-} mice after eight weeks of HFD feeding after a five-hour fast followed by gavaging of a bolus of glucose (2 g/kg). n=10-13.

(E) Blood glucose during intraperitoneal glucose tolerance tests and area-under-curve of the tests in WT and *Rag2*^{-/-}; *Il2rg*^{-/-} mice after nine weeks of HFD feeding fasted for five hours followed by an intraperitoneal injection of a bolus of glucose (2 g/kg). n=10-14.

(F) Blood glucose during insulin tolerance tests in WT and *Rag2*^{-/-}; *Il2rg*^{-/-} mice after ten weeks of HFD feeding fasted for five hours followed by an intraperitoneal injection of a bolus of insulin (0.7 unit/kg). n=10-14.

(G) Body weight of HFD-fed WT and *Rag2*^{-/-}; *Il2rg*^{-/-} mice over twelve weeks of high-fat diet feeding. n=10-14.

(H) Fat and lean mass of WT and *Rag2*^{-/-}; *Il2rg*^{-/-} mice after eleven weeks of HFD feeding. n=10-14.

(I) Energy expenditure of WT and *Rag2*^{-/-}; *Il2rg*^{-/-} mice after eleven weeks of HFD feeding as measured in metabolic cages. n=8-13.

(J) Average locomotor activity of WT and *Rag2*^{-/-}; *Il2rg*^{-/-} mice after eleven weeks of HFD feeding as measured in metabolic cages. n=8-13.

(K) Average daily food and water intake of WT and *Rag2*^{-/-}; *Il2rg*^{-/-} mice after eleven weeks of HFD feeding as measured in metabolic cages. n=10-14.

(L) Organ weights of WT and *Rag2*^{-/-}; *Il2rg*^{-/-} mice after twelve weeks of HFD feeding. n=10-14.

(M) Expression of *Glp1r* in the lungs and atria of *Glp1r*[Tcell+/+] and *Glp1r*[Tcell-/-] mice. n=5-12.

(N) Left panel: representative images of CD3 staining by immunohistochemistry in *Glp1r*[Tcell+/+] and *Glp1r*[Tcell-/-] mouse jejuna. Scale bar=100 μm. Right panel: density of CD3^{+} cells in *Glp1r*[Tcell+/+] and *Glp1r*[Tcell-/-] mouse jejuna. n=5-9.

(O) The composition of gut IELs based on CD4 and CD8 expression in *Glp1r*[Tcell+/+] and *Glp1r*[Tcell-/-] mice. n=4-10.

(P) The composition of gut IEL subtypes based on CD8 dimer and TCR expression in *Glp1r*[Tcell+/+] and *Glp1r*[Tcell-/-] mice. n=4-10.

(Q) Plasma insulin levels of chow-fed *Glp1r*[Tcell+/+] and *Glp1r*[Tcell-/-] mice after a five-hour fast followed by gavaging of a bolus of glucose (2 g/kg). n=7-8.

(R) Plasma insulin levels of *Glp1r*[Tcell+/+] and *Glp1r*[Tcell-/-] mice after eight weeks of HFD feeding fasted for five hours followed by gavaging of a bolus of glucose (2 g/kg). n=12-15.

(S) Blood glucose during intraperitoneal glucose tolerance tests and area-under-curve of the tests in $Glp1r^{Tcell+/+}$ and $Glp1r^{Tcell-/-}$ mice after nine weeks of HFD feeding fasted for five hours followed by an intraperitoneal injection of glucose (2 g/kg). n=9-13.

(T) Blood glucose during insulin tolerance tests in $Glp1r^{Tcell+/+}$ and $Glp1r^{Tcell-/-}$ mice after ten weeks of HFD feeding fasted for five hours followed by an intraperitoneal injection of insulin (0.7 unit/kg). n=9-13.

(U) Body weight of $Glp1r^{Tcell+/+}$ and $Glp1r^{Tcell-/-}$ mice over twelve weeks of HFD feeding. n=15-17.

(V) Fat and lean mass of $Glp1r^{Tcell+/+}$ and $Glp1r^{Tcell-/-}$ mice after eleven weeks of HFD feeding. n=9-12.

(W) Energy expenditure of $Glp1r^{Tcell+/+}$ and $Glp1r^{Tcell-/-}$ mice after eleven weeks of HFD feeding as measured in metabolic cages. n=11-12.

(X) Total distance travelled by $Glp1r^{Tcell+/+}$ and $Glp1r^{Tcell-/-}$ mice after eleven weeks of HFD feeding as measured in metabolic cages. n=11-12.

(Y) Average daily food and water intake of $Glp1r^{Tcell+/+}$ and $Glp1r^{Tcell-/-}$ mice after eleven weeks of HFD feeding as measured in metabolic cages. n=7-12.

Data are represented as mean ± SD. * $p < 0.05$ ** $p < 0.01$ *** $p < 0.001$ *** $p < 0.0001$. Student's t tests were used in Figures S1B, S1E, S1F, S1H, S1L, S1P, S1V, and S1Y. Two-way ANOVA tests were used in Figure S1C and S1U.

Abbreviations: NEFA: non-esterified fatty acid; TG: triglyceride. LTT: lipid tolerance test; HFD: high fat diet; OGTT: oral glucose tolerance test; ipGTT: intraperitoneal glucose tolerance test; ITT: insulin tolerance test; iBAT: interscapular brown adipose tissue; gWAT: gonadal white adipose tissue; scWAT: subcutaneous white adipose tissue
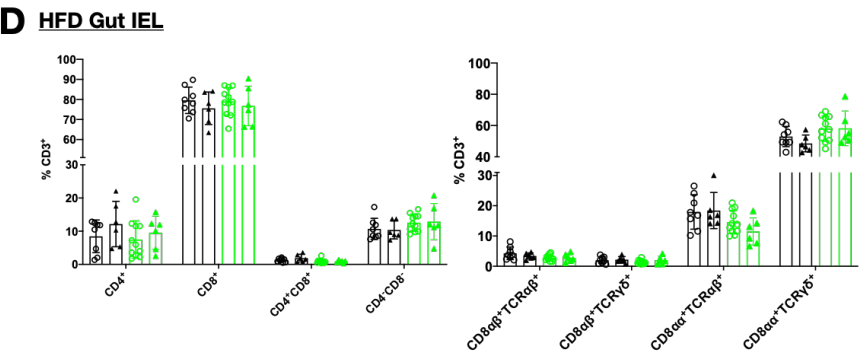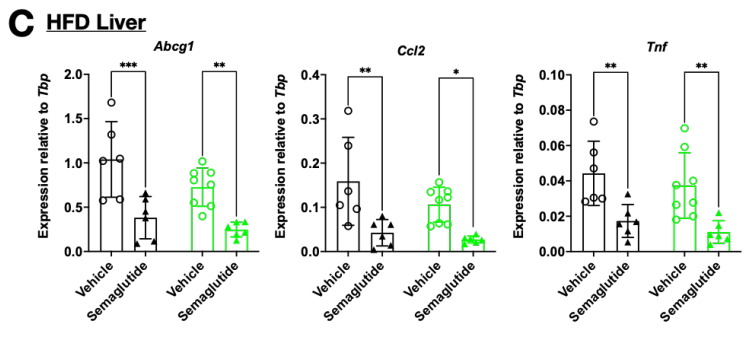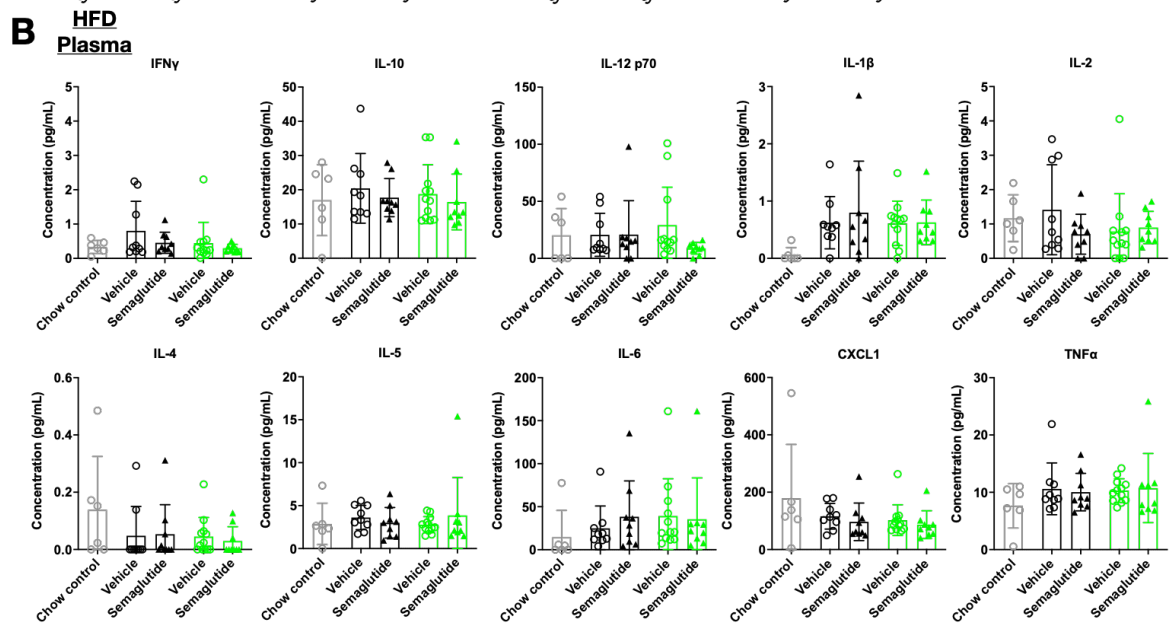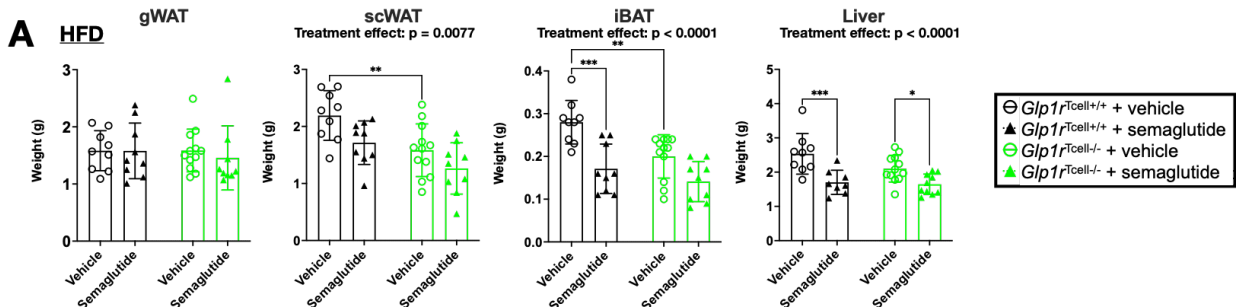
Figure S2, related to Figure 2. Effects of semaglutide on tissue biometry and inflammation in HFD-fed $Glp1r^{Tcell-/-}$ mice.

(A) Organ weights of HFD-fed $Glp1r^{Tcell+/+}$ and $Glp1r^{Tcell-/-}$ mice after one week of semaglutide (10 μg/kg) treatment. n=9-12.

(B) Plasma cytokine levels in HFD-fed $Glp1r^{Tcell+/+}$ and $Glp1r^{Tcell-/-}$ mice after one week of semaglutide (10 μg/kg) treatment. Age-matched $Glp1r^{Tcell+/+}$ mice were shown as chow controls. n=6-12.

(C) Expression of genes linked to inflammation (*Ccl2*, *Tnf*) and lipid metabolism (*Abcg1*) in the livers of HFD-fed $Glp1r^{Tcell+/+}$ and $Glp1r^{Tcell-/-}$ mice after one week of semaglutide (10 μg/kg) treatment. n=5-8.

(D) The composition of gut IELs in HFD-fed $Glp1r^{Tcell+/+}$ and $Glp1r^{Tcell-/-}$ mice after one week of semaglutide (10 μg/kg) treatment. n=6-11.

Data are represented as mean ± SD. * $p < 0.05$ ** $p < 0.01$ *** $p < 0.001$. Two-way ANOVA tests were used in Figures S2A and S2C.
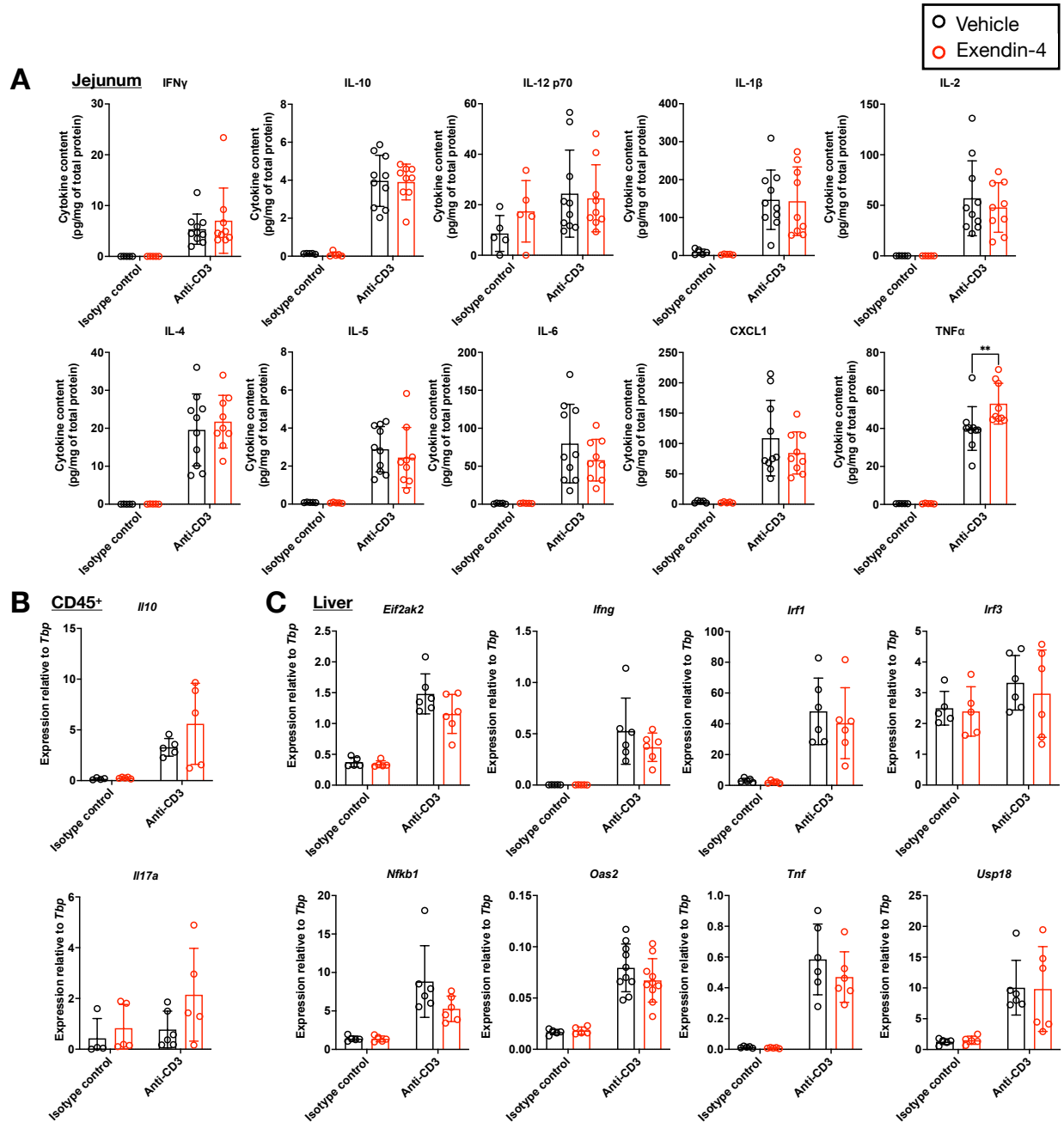
Figure S3, related to Figure 3. Effects of exendin-4 on tissue cytokine content in anti-CD3-treated C57BL/6J mice.
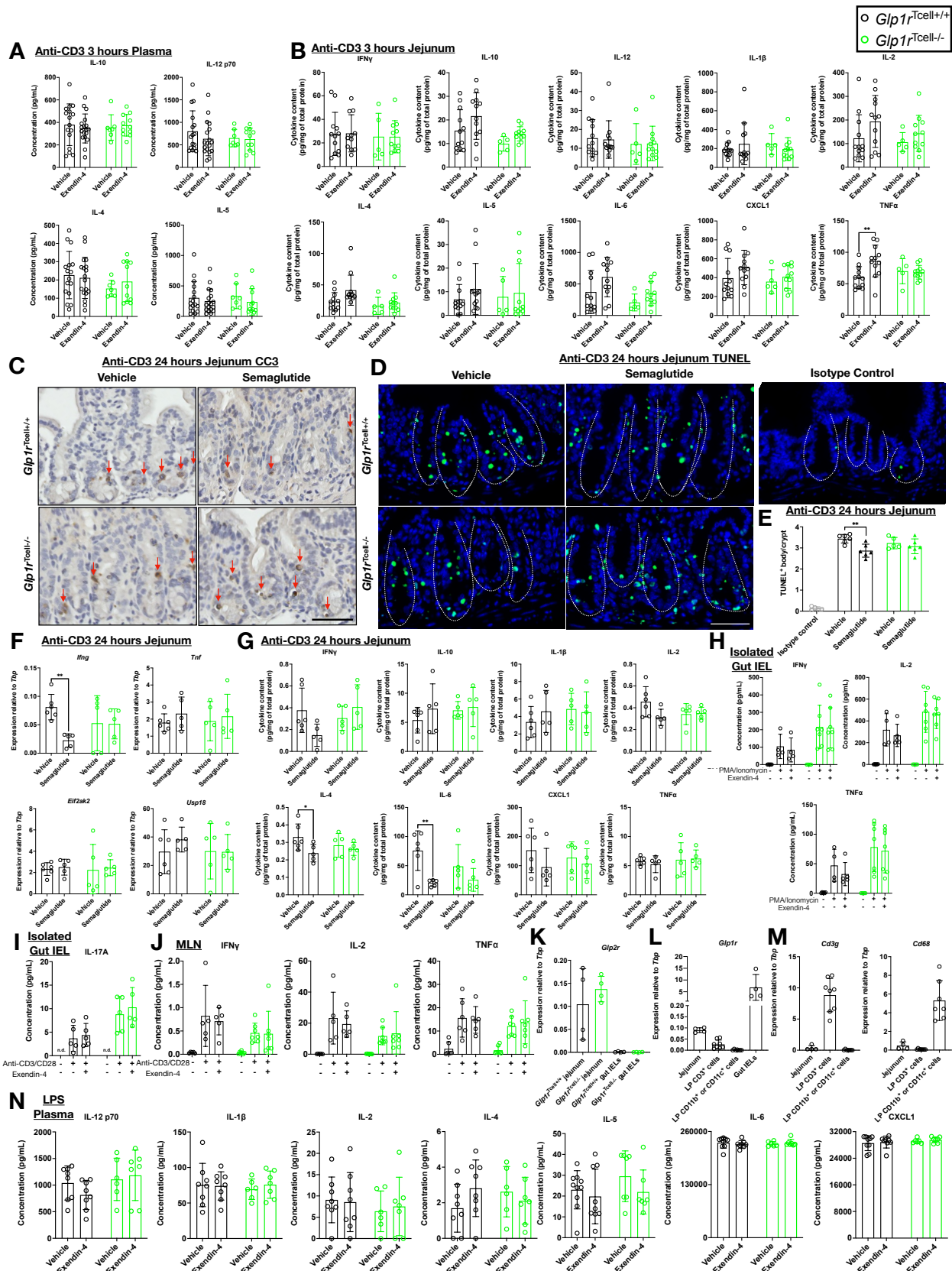(A) Jejunal cytokine protein contents in C57BL/6J mice treated with anti-CD3 and exendin-4 (10 nmol/kg). n=5-10.
(B) Expression of *Il10* and *Il17a* in gut IELs sorted from the small intestine of C57BL/6J mice treated with anti-CD3 and exendin-4 (10 nmol/kg) for three hours. n=4-5.
(C) Expression of cytokine and interferon-stimulated genes in the liver of C57BL/6J mice treated with anti-CD3 and exendin-4 (10 nmol/kg) for three hours. n=5-6.

Data are represented as mean ± SD. ** $p < 0.01$. Two-way ANOVA tests were used in Figure S3A.

A Anti-CD3 3 hours Plasma

B Anti-CD3 3 hours Jejunum

C Anti-CD3 24 hours Jejunum CC3

D Anti-CD3 24 hours Jejunum TUNEL

E Anti-CD3 24 hours Jejunum

F Anti-CD3 24 hours Jejunum

G Anti-CD3 24 hours Jejunum

H Isolated Gut IEL

I Isolated Gut IEL

J MLN

K

L

M

N LPS Plasma

Legend: $Glp1r^{Tcell+/+}$ (black), $Glp1r^{Tcell-/-}$ (green)

Figure S4, related to Figure 4. Effects of exendin-4 and semaglutide on anti-CD3-treated *Glp1r*$^{Tcell-/-}$ mice.

(A) Plasma cytokine levels in *Glp1r*$^{Tcell+/+}$ and *Glp1r*$^{Tcell-/-}$ mice treated with anti-CD3 and exendin-4 (10 nmol/kg) for three hours. n=7-17.

(B) Jejunal cytokine content of *Glp1r*$^{Tcell+/+}$ and *Glp1r*$^{Tcell-/-}$ mice treated with anti-CD3 and exendin-4 (10 nmol/kg) for three hours. n=5-10.

(C) Representative images of cleaved caspase-3 staining by immunohistochemistry in the jejunum of *Glp1r*$^{Tcell+/+}$ and *Glp1r*$^{Tcell-/-}$ mice treated with anti-CD3 and semaglutide (10 µg/kg) for 24 hours. The red arrows denote the cleaved cascade 3-positive bodies. Scale bar=50 µm.

(D) Representative images of TUNEL staining by immunofluorescence in the jejunum of *Glp1r*$^{Tcell+/+}$ and *Glp1r*$^{Tcell-/-}$ mice treated with anti-CD3 and semaglutide (10 µg/kg) for 24 hours. Blue: DAPI. Green: TUNEL. The dotted lines denote the position of the crypts. Scale bar=50 µm.

(E) Density of TUNEL-positive bodies as quantified by immunofluorescence in the jejunum of *Glp1r*$^{Tcell+/+}$ and *Glp1r*$^{Tcell-/-}$ mice treated with anti-CD3 and semaglutide (10 µg/kg) for 24 hours. n=5-6.

(F) Expression of *Ifng*, *Tnf*, *Eif2ak2*, and *Usp18* in the jejunum of *Glp1r*$^{Tcell+/+}$ and *Glp1r*$^{Tcell-/-}$ mice treated with anti-CD3 and semaglutide (10 µg/kg) for 24 hours. n=5-6.

(G) Jejunal cytokine content of *Glp1r*$^{Tcell+/+}$ and *Glp1r*$^{Tcell-/-}$ mice treated with anti-CD3 and semaglutide (10 µg/kg) for 24 hours. n=5-6.

(H) Secreted cytokine levels from sorted *Glp1r*$^{Tcell+/+}$ and *Glp1r*$^{Tcell-/-}$ mouse gut IELs treated with PMA/ionomycin and exendin-4 (50 nM) for 5 hours *ex vivo*. n=4-7.

(I) Secreted IL-17A levels from *Glp1r*$^{Tcell+/+}$ and *Glp1r*$^{Tcell-/-}$ mouse gut IELs treated with anti-CD3/anti-CD28 and exendin-4 (50 nM) for 5 hours *ex vivo*. n=5.

(J) Secreted cytokine levels from sorted *Glp1r*$^{Tcell+/+}$ and *Glp1r*$^{Tcell-/-}$ mouse MLN cells treated with anti-CD3/anti-CD28 and exendin-4 (50 nM) for 5 hours *ex vivo*. n=6.

(K) Expression of *Glp2r* in the jejunum and gut IELs isolated from *Glp1r*$^{Tcell+/+}$ and *Glp1r*$^{Tcell-/-}$ mice. n=4-8.

(L) Expression of *Glp1r* in the jejunum, gut lamina propria T cells, gut lamina propria phagocytes, and gut IELs isolated from C57BL/6J mice. n=4-8.

(M) Expression of *Cd3g* and *Cd68* in the jejunum, gut lamina propria T cells, and phagocytes isolated from C57BL/6J mice. n=4-8.

(N) Plasma cytokine levels in *Glp1r*$^{Tcell+/+}$ and *Glp1r*$^{Tcell-/-}$ mice treated with LPS and exendin-4 (10 nmol/kg) for three hours. n=7-8.

Data are represented as mean ± SD. * $p < 0.05$ ** $p < 0.01$. Two-way ANOVA tests were used in Figures S4B, S4E, S4F, and S4G.

Abbreviations: CC3: cleaved caspase 3; MLN: mesenteric lymph node; LP: lamina propria.
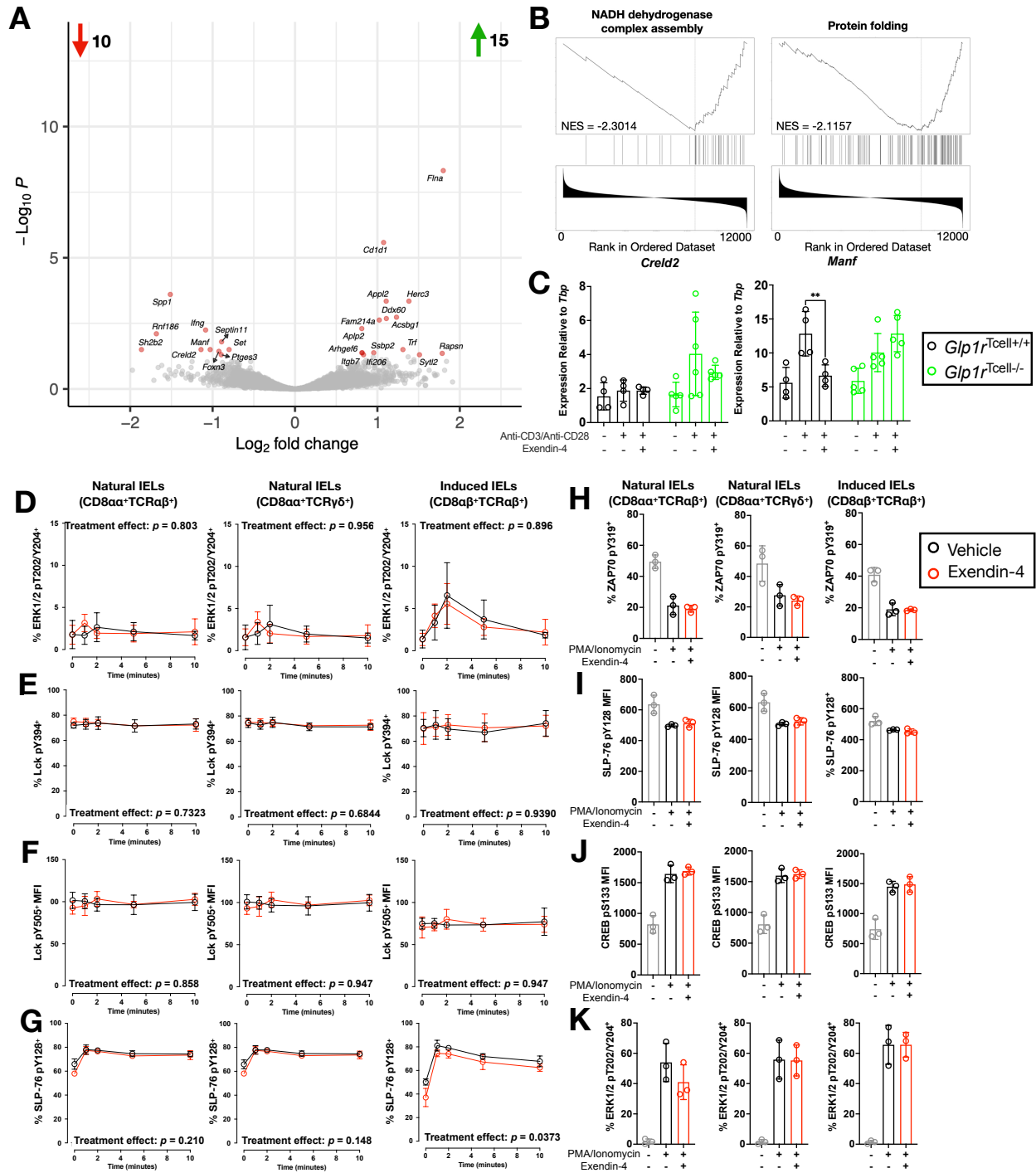
Figure S5, related to Figure 5. Transcriptomic analyses and phosphorylation events of activated gut IELs treated with exendin-4.
(A) A volcano plot illustrating the differentially expressed genes (red dots in the plot) in gut IELs isolated from C57BL/6J mice treated with vehicle or exendin-4 (10 nmol/kg) plus anti-CD3 for three hours as detected by RNA-seq. The number next to the red

arrow shows the number of significantly downregulated genes, and the number next to the green arrow shows the number of significantly upregulated genes. n=4.

(B) Gene set enrichment analysis for Biological Process GO terms in all genes detected in the RNA-seq data. Two gene sets are shown as an example. NES stands for normalized enrichment score. A negative NES indicates that the genes associated with the given GO term in the dataset trend towards downregulation.

(C) Expression of *Creld2* and *Manf* in sorted *Glp1r*$^{Tcell+/+}$ and *Glp1r*$^{Tcell-/-}$ mouse gut IELs treated with anti-CD3/anti-CD28 and exendin-4 (50 nM) for five hours. n=4-5.

(D, E, and F) Flow cytometric analyses on the phosphorylation of (D) ERK1/2 T202/Y204, (E) Lck Y394 and (F) Lck Y505 in sorted C57BL/6J mouse gut IELs activated with anti-CD3/anti-CD28 and treated with exendin-4 (50 nM). n=3 independent experiments.

(G) Flow cytometric analyses on the proportion of SLP-76 pY128$^+$ cells in sorted C57BL/6J mouse gut IELs activated with anti-CD3/anti-CD28 and treated with exendin-4 (50 nM). n=3 independent experiments.

(H, I, J, & K) Flow cytometric analyses on the phosphorylation of (H) ZAP-70 Y319, (I) SLP-76 Y128, (J) CREB S133, and (K) ERK1/2 T202/Y204 in sorted C57BL/6J mouse gut IELs pretreated with exendin-4 (50 nM) for five minutes followed by activation with PMA/ionomycin for ten minutes. n=3 independent experiments.

Data are represented as mean ± SD. ** $p < 0.01$. Two-way ANOVA tests were used in Figure S5C. Two-way ANOVA tests were used in Figures S5D, S5E, S5F, and S5G.

Abbreviations: MFI: median fluorescence intensity.